Role of Lattice Oxygen in Methane Activation on Ni-Phyllosilicate@$Ce_{1-x}Zr_xO_2$ Core-shell Catalyst for Methane Dry Reforming: Zr Doping Effect, Mechanism, and Kinetic Study.

Sonali Das[a], Ashok Jangam[a], Shanmukapriya Jayaprakash[a], Shibo Xi[b], Kus Hidajat[a], Keiichi Tomishige[c], Sibudjing Kawi[a]*

[a] Department of Chemical and Biomolecular Engineering, National University of Singapore, Singapore 119260, Singapore

[b] Institute of Chemical and Engineering Sciences, A*STAR, 1 Pesek Road, Jurong Island, 627833, Singapore

[c]Department of Applied Chemistry, School of Engineering, Tohoku University, Aoba 6-6-07, Aramaki, Aoba-ku, Sendai, Japan

*Sibudjing Kawi

E-mail address: chekawis@nus.edu.sg

Tel.: +65 6516 6312; fax: +65 6779 1936.

Graphical Abstract

Highlights

- Core-shell Ni-phyllosilicate@$Ce_{1-x}Zr_xO_2$ catalysts with high coke resistance for DRM
- Optimum Zr doping in shell doubles catalyst activity (TOF) in DRM
- TOF increase upon Zr doping caused by higher lattice oxygen content of shell and SMSI
- Mechanism & kinetic study conducted to probe role of lattice oxygen in DRM activity
- Lattice oxygen of $Ce_{1-x}Zr_xO_2$ facilitates CH_4 dissociation at metal/support interface

ABSTRACT

Sandwich structured core-shell Ni-Phyllosilicate@$Ce_{1-x}Zr_xO_2$ catalysts with high coke resistance and activity are reported for DRM. Optimal Zr loading (x = 0.05 – 0.1) in the $Ce_{1-x}Zr_xO_2$ shell is observed to significantly increase the intrinsic activity for DRM. Extensive catalyst

characterization using HRTEM, XRD, TPR, O_2-TPD, XPS, EXAFS and CO pulse chemisorption indicates that the enhancement in DRM activity upon Zr doping can be attributed to the increase in lattice oxygen mobility of the ceria-zirconia shell and stronger metal-support interaction with Ni. It is inferred from a rigorous kinetic and mechanism study that the lattice oxygen of $Ce_{1-x}Zr_xO_2$ not only participates in the oxidation of carbonaceous reaction intermediates but also facilitates the rate determining step of C-H bond dissociation of CH_4 on Ni by an oxygen-mediated dissociation pathway. The involvement of lattice oxygen in methane activation and dissociation manifests in the higher DRM activity of the Zr-doped catalyst with maximum oxygen storage capacity.

KEYWORDS: Dry reforming of methane, redox mechanism, ceria-zirconia, mechanism and kinetics, methane activation.

1. INTRODUCTION

With ever-increasing demand for energy, fuels and commodity chemicals, the catalytic activation and conversion of methane from natural gas or shale gas reserves has drawn significant attention both in academia and industry. Out of the several technologies to convert methane, dry reforming of methane is of particular research and industrial interest, because it can recycle carbon dioxide by using it as a raw material. In DRM (Eq. 1), methane and CO_2 are converted into syngas with an ideal H_2/CO ratio of one. The syngas product from DRM can be used as a source of hydrogen, as a fuel to generate power or as a raw material for higher chemical synthesis. DRM is conducted at high temperatures (600 – 1000^{o}C) because of the endothermicity of the reaction. The main

DRM reaction is accompanied by several side reactions (Eq. 2-4) that affect the product composition. Deposition of solid carbonaceous species or coke can happen both from the complete decomposition of methane to hydrogen and coke (Eq. 3) or the disproportionation of CO to form CO_2 and coke (Eq. 4).

$$CH_4 + CO_2 \rightarrow 2CO + 2H_2 \qquad \Delta H^o = 247.3\ kJ\ mol^{-1} \qquad (1)$$

$$H_2 + CO_2 \leftrightarrow CO + H_2O \qquad \Delta H^o = 41\ kJ\ mol^{-1} \qquad (2)$$

$$CH_4 \rightarrow C_{ads} + 2H_2 \qquad \Delta H^o = 75\ kJ\ mol^{-1} \qquad (3)$$

$$2CO \leftrightarrow C_{ads} + CO_2 \qquad \Delta H^o = -172\ kJ\ mol^{-1} \qquad (4)$$

Nickel is highly promising as a relatively inexpensive and abundant non-noble metal catalyst with high activity for DRM. However, a major issue with Ni-based catalysts is its rapid deactivation because of coke formation and metal sintering [1], which limits the feasibility of its large-scale industrial implementation.

Core-shell structured catalysts have recently emerged as promising candidates for stable coke-resistant catalysts for DRM with good resistance to metal sintering [2-4]. In a core-shell structured catalyst, the active nanoparticles can be encapsulated by a coating of thermally stable material which physically hinders particle migration and sintering [5]. A core-shell structure can also be used to combine complementary catalytic functions to accelerate the removal of coke precursors in DRM. In our previous work, we developed a bifunctional sandwiched multicore-shell Ni-SiO_2@CeO_2 catalyst, where the cerium oxide shell played the role of both a protective physical barrier on the Ni nanoparticles and of an active metal oxide supplying surface lattice oxygen for the oxidation of nascent coke on the Ni surface [6]. Cerium oxide has good redox

properties and can undergo substantial oxygen stoichiometric changes by switching between Ce^{4+} and Ce^{3+}, thereby acting as a source or sink for oxygen involved in reactions on the ceria surface. Extensive mechanistic studies by Efstathiou's group have unambiguously demonstrated carbon oxidation and CO formation through the reaction of support lattice oxygen on Ce-containing catalysts in DRM [7-11]. Small particle size of the metal nanoparticles and strong interaction between the metal and ceria is necessary to obtain the promotional effect of the support in preventing coke accumulation [12].

Addition of zirconia to cerium oxide is a commonly used strategy to improve its oxygen storage/ transport properties and thermal resistance. Incorporation of Zr^{4+} in the CeO_2 lattice has been reported to facilitate the partial reduction of Ce^{4+} to Ce^{3+} and the formation of oxygen vacancies by creating lattice distortion [13, 14]. The increase in lattice defects and oxygen vacancies has a positive effect on the oxygen ion (O^{2-}) mobility and oxygen release capacity of the mixed oxide. Ceria-zirconia supported catalysts have been frequently investigated for DRM [13-17]. Kambolis et al. [14] investigated the performance of supported Ni catalysts on CeO_2-ZrO_2 (100% - 28% Ce) carriers in DRM and observed higher reactant conversions on Zr doped catalysts. However, no direct correlation could be found between the rate of coke deposition during DRM and the extent of Zr doping in the support. Laosiripojana et al. [18] studied Ni supported on high surface area ceria-zirconia for steam reforming of methane and observed that a Ce/Zr molar ratio of 3:1 was optimum for high catalytic activity and stability. Versiliades et al. [11] reported a two-fold influence of lattice oxygen of Ni/$Ce_xPr_{1-x}O_2$ catalysts and observed that its effect on carbon accumulation during DRM was significantly larger than that on CH_4/CO_2 conversion rates. Another study by Wolfbeisser and co-workers [15] on Ni/CeO_2-ZrO_2 catalysts concluded that the catalyst activity strongly depends on synthesis method of the ceria-zirconia support and the

resulting phase composition, rather than on nominal composition of the catalyst. A recent investigation into the effect of Zr doping in Ni/CeO_2 on DRM performance using advanced characterization techniques concluded that addition of Zr increases the reducibility of Ni, maintains smaller Ni particle size and suppresses the migration of Ni from the surface into the CeO_2 lattice [16]. Makri et al. [19] investigated the effect of doping Zr and Pr in $Ni/Ce_{1-x}M_xO_2$ ($M=Zr^{4+}$ or Pr^{3+}) catalysts and reported a sharp decrease in conversion when Zr mole fraction was increased from 0.2 to 0.5 in $Ni/Ce_{1-x}Zr_xO_2$ catalyst. On the other hand, Damyanova et al. [17] reported a monotonic increase in DRM activity with increase in Zr content on Pt/CeO_2-ZrO_2 catalysts. Thus, although ceria-zirconia has been frequently studied as an effective support for DRM catalysts, there is wide disparity in the reported performance of these catalysts in DRM, both in terms of the activity and stability. Such discrepancies often stem from the complex dependence of catalytic properties on not only the material composition but also the chemical states of the various active components, metal-support interaction, metal dispersion, reaction conditions and so on.

This study aims at unraveling the fundamental mechanistic correlations between the DRM activity and the oxygen storage capacity of bifunctional ceria-zirconia containing core-shell catalysts. Here, we have developed core-shell $Ni\text{-}PS@Ce_{1-x}Zr_xO_2$ catalysts with a nickel phyllosilicate (Ni-PS) core and a ceria-zirconia shell and varied the Zr loading in the shell in an attempt to adjust the oxygen transport properties of the catalyst and the metal-support interaction. The unique catalyst structure consists of highly dispersed Ni nanoparticles (formed by the reduction of nickel phyllosilicate) sandwiched between a silica support and a ceria-zirconia shell. We observed that a small amount of Zr loading in the ceria-zirconia shell increased the DRM activity of the $Ni\text{-}PS@Ce_{1-x}Zr_xO_2$ catalyst significantly. Coke formation was negligible on all the

studied catalysts irrespective of the Zr doping, by virtue of the core-shell morphology and bi-functional nature of the catalyst. The core-shell morphology allows us to decouple and exclude some of the effects of Zr loading on the physicochemical properties of the catalyst, such as sintering and coke-resistance, and provides unique opportunities to investigate the catalytic phenomena more fundamentally. The role of redox supports like ceria-zirconia in increasing coke-resistance in DRM by the participation of support lattice oxygen in the carbon oxidation pathway is well-studied in literature [6-9, 11, 20]. However, the fundamental correlation between intrinsic catalytic activity or TOF and the physicochemical properties of ceria-zirconia has not been clearly established.

In this study, we aim to experimentally demonstrate the mechanistic dependence of catalytic activity in DRM on the lattice oxygen of the support in core-shell catalysts. Detailed catalyst characterization is done to understand the relation between the Zr content and DRM performance of the core-shell catalysts, and a rigorous mechanism and kinetic study is conducted on the Ni-PS@$Ce_{0.9}Zr_{0.1}O_2$ catalyst to understand the effect of the physicochemical properties of the catalyst on the intrinsic kinetics and mechanism.

2. EXPERIMENTAL SECTION

2.1. Catalyst Synthesis

The Ni-PS core was synthesized by ammonia evaporation method using Stöber silica as support, as reported earlier [6]. 2 g of Stöber silica nano-spheres were dispersed in a solution of 280 ml ethanol and 50 ml water. Appropriate amount of nickel nitrate hexahydrate was added to the solution and the pH was adjusted to 10 by adding ammonium hydroxide solution (25%). The solution was stirred in a water bath at 70^{o}C to evaporate the ammonia. The solid residue was then

recovered by centrifuging the mixture followed by washing and drying overnight at 60°C. $Ce_{1-x}Zr_xO_2$ shell was coated on the Ni-PS nanospheres by a precipitation method. Cerium nitrate hexahydrate and zirconium oxynitrate hydrate were used as the precursors for Ce and Zr, respectively. 500 mg of Ni-PS nanospheres was dispersed in 80 ml ethanol, and appropriate amount of Ce and Zr salts were added, followed by stirring for 2 h. The total loading of Ce and Zr salts was fixed at 3 mmol/g Ni-PS core. An aqueous solution of 10 g hexamethylenetetramine was added to the dispersion and stirred at 70°C for 7 h. The sample was then centrifuged, washed, dried at 60°C, and calcined at 600°C for 4 h. $SiO_2@Ce_{1-x}Zr_xO_2$ reference samples were synthesized by same method by replacing Ni-PS with Stöber silica nano-spheres.

$Ce_{0.9}Zr_{0.1}O_2$ was synthesized as a reference material for control experiments by co-precipitation method. Appropriate amounts of cerium nitrate hexahydrate and zirconium oxynitrate hydrate were dissolved in DI water, and aqueous NaOH solution was added under vigorous stirring until 10.5 pH. The precipitate was washed thoroughly, dried at 60°C, and calcined at 600°C for 4 h.

2.2. Catalyst Characterization

HRTEM images of catalysts after calcination, reduction and DRM reaction were taken on a JEOL JEM-2100 microscope. Crystallographic phases in the fresh and reduced catalysts were characterized by XRD scan with a Shimadzu XRD-6000 X-ray diffractometer with a Cu K-α as X-ray source. The lattice parameters of fluorite structure were estimated by Rietveld refinement of the obtained XRD patterns of the calcined catalysts using FullProf software.

H_2-TPR was conducted on a Thermo Scientific TPDRO 1100 series system equipped with a TCD. 30 mg of fresh catalyst was heated in 5% H_2-N_2 (30 ml/min) at a ramp rate of 10°C/min to obtain H_2-TPR profiles. O_2-TPD was also performed in the same TPDRO system and the outlet

gas was analyzed by a Shimadzu mass spectrometer (GCMS-QP2010, with the GC bypassed). A fixed weight of fresh catalyst was reduced at 750^{o}C for 1 h in 5% H_2-N_2 (30 ml/min) followed by cooling to the 600^{o}C in He and O_2 flow (30 ml/min) at 600^{o}C for 1 h. The treated sample was subsequently cooled down to room temperature in O_2, followed by He purge. The temperature was ramped in He flow from 50^{o}C to 850^{o}C at 10^{o}C/min, and the product was analyzed by MS.

The exposed Ni surface area in the reduced catalysts was measured by CO pulse chemisorption in the same TPDRO equipment. The Ni-PS@$Ce_{1-x}Zr_xO_2$ catalysts were reduced at 750^{o}C for 1 h in 5% H_2-N_2 mixture and cooled down to 30^{o}C in same gas. After purging with He, pulses of pure CO were subsequently injected at 30^{o}C until saturation of the metal surface. SiO_2@$Ce_{1-x}Zr_xO_2$ samples (without Ni) were also subjected to the same treatment, and the amount of CO chemisorbed on these samples were subtracted from that on the Ni-PS@$Ce_{1-x}Zr_xO_2$ catalysts to determine the CO uptake on Ni. The specific Ni surface area was determined from the moles of chemisorbed CO assuming one CO molecule is adsorbed per surface Ni atom [21].

Ni K-edge XAS of catalysts were performed at XAFCA beamline of Singapore Synchrotron Light Source under transmission mode. Pellets were prepared with the calcined catalyst diluted with boron nitride, followed by reduction at 750^{o}C. The reduced pellets were handled in glove box in inert atmosphere and transferred to an enclosed EXAFS holder for measurement. Athena was used for data normalization and linear combination fitting of the XANES spectra, and Artemis was used to do the fitting of the EXAFS spectra. Ni foil was used for energy calibration. XPS spectra of the reduced catalysts for Ce 3d were obtained in a Kratos AXIS spectrometer using Al Kα X- ray source (energy = 1486.6 eV). The reduced samples were briefly exposed to air before XPS analysis. The spectra were calibrated by setting C1s reference signal at 284.5 eV.

The elemental composition of the fresh catalysts was measured by a Thermal Scientific iCAP 6000 ICP-OES A fixed mass of the sample was digested in an aqueous solution of HNO_3, HF and H_2O_2 under ultrasonication. Standard solutions with appropriate concentrations of Ni, Ce and Zr were used for calibration. The specific surface area of the reduced and spent catalysts was measured from N_2 adsorption/desorption experiments at 77K on an ASAP 2020 instrument and calculated by BET method. Sample degassing before analysis was done by heating the catalyst under vacuum (500 µmHg) for 8 h at 300 °C.

The amount of coke on the spent catalyst after DRM reaction was measured by TGA on a Shimadzu DTG-60 thermogravimetric analyzer.

2.3. Catalyst Evaluation

The catalyst performance in DRM reaction was tested in a 4 mm ID quartz reactor heated by a Carbolite digital furnace connected to an online Agilent 7820A gas chromatograph equipped with a TCD for product analysis. The specific activity of the catalyst and turnover frequency (TOF) was measured at a WHSV of 200 $Lh^{-1}g^{-1}$, CH_4: CO_2 ratio of 1:1, 600ºC and 1 bar pressure. Catalyst reduction was performed *in situ* before reaction in a pure H_2 (20 ml/min) at 750ºC for 1 h. Specific activity was calculated as follows:

$$Activity, CH_4\left(\frac{mol}{min\ g_{Ni}}\right) = \frac{inlet\ CH_4 - outlet\ CH_4\left(\frac{mol}{min}\right)}{catalyst\ amount\ (g) * Ni\ loading\ \left(\frac{g_{Ni}}{g}\right)} \quad (5)$$

$$Activity, CO_2(\frac{mol}{min\ g_{Ni}}) = \frac{inlet\ CO_2 - outlet\ CO_2\left(\frac{mol}{s}\right)}{catalyst\ amount\ (g) * Ni\ loading\ \left(\frac{g_{Ni}}{g}\right)} \quad (6)$$

Turnover frequency (TOF) for methane conversion was calculated as:

$$TOF, CH_4(s^{-1}) = \frac{inlet\ CH_4 - outlet\ CH_4\left(\frac{mol}{s}\right)}{catalyst\ amount\ (g) * specific\ moles\ of\ surface\ metal^a\ \left(\frac{mol}{g}\right)} \quad (7)$$

[a]based on CO pulse chemisorption results.

A stability test was conducted on Ni-PS@$Ce_{0.9}Zr_{0.1}O_2$ at 600 and 800°C, 1 bar pressure, CH_4: CO_2: He ratio of 1:1:1 and a WHSV of 18 $Lh^{-1}g^{-1}$ for 96 h.

$$CH_4\ conversion = \frac{inlet\ CH_4 - outlet\ CH_4\ (mols/min)}{inlet\ CH_4\ (mols/min)}\ x\ 100\% \quad (8)$$

$$CO_2\ conversion = \frac{inlet\ CO_2 - outlet\ CO_2\ (mols/min)}{inlet\ CO_2\ (mols/min)}\ x\ 100\% \quad (9)$$

$$H_2/\ CO = \frac{outlet\ H_2\ (mols/min)}{outlet\ CO\ (mols/min)} \quad (10)$$

2.4. Mechanism Study

In situ DRIFTS was conducted in a Bruker FTIR Vertex 70 spectrometer using a Harrick Praying Mantis DRIFTS gas cell. The Ni-PS@$Ce_{0.9}Zr_{0.1}O_2$ catalyst was pre-reduced at 750°C for 1 h and then reduced *in situ* in the DRIFTS cell at 600°C, followed by flushing with He. Background collection was done in He flow at 600°C. Pulses of CH_4 and CO_2 were introduced in the sequence of $CH_4 \rightarrow CO_2 \rightarrow CH_4$ with continuous He flow at 10-minute intervals. IR spectra were collected every 15s (repeated 32 times, resolution of 4 cm^{-1}).

Transient response of CO and CO_2 formation upon introduction of CH_4 on the Ni-PS@CeO_2 and Ni-PS@$Ce_{0.9}Zr_{0.1}O_2$ was analyzed by mass spectrometer (Shimadzu GCMS-QP2010.). A fixed amount of catalyst was loaded in a packed bed reactor, reduced at 750°C in H_2 for 1 h, and then

cooled to 600ºC in flowing He. After purging with He, the inlet flow was changed to 10% CH_4/ He (30 ml/min) and the transient reactant/ product profiles were analyzed by MS.

CH_4-TPSR (Temperature Programmed Surface Reaction) was conducted on Ni-PS and Ni-PS@$Ce_{0.9}Zr_{0.1}O_2$ catalysts in the same set-up. A fixed mass of calcined catalyst was reduced at 750ºC in pure H_2 for 1 h and cooled to room temperature in He. A mixture of 5 ml/min CH_4 and 25 ml/min Ar was introduced into the reactor and the temperature was ramped from room temperature to 800ºC at 3ºC/min. The outlet gas was continuously monitored by MS. A control experiment was also conducted using a $Ce_{0.9}Zr_{0.1}O_2$ sample without any Ni loading.

Pulse experiments were conducted on the Ni-PS@$Ce_{0.9}Zr_{0.1}O_2$ catalyst in the same packed bed reactor connected to MS. A fixed weight of the catalyst was reduced at 750ºC, followed by cooling to 600ºC under He flow (15 ml/min). Pulses of fixed volume (0.3 ml) were introduced into the inlet He stream in the following sequence: 1. five pulses of $^{13}CH_4$ (pulse #1-5), 2. three pulses of $^{12}CO_2$ (pulse #6-8), 3. three pulses of $^{13}CH_4$ (pulse #9-11), 4. three pulses of H_2 (pulse #12-14), and 5. three pulses of $^{13}CH_4$ (pulse #15-17). The reactor temperature was maintained at 600ºC. The mass spectra for m/z = 2, 17, 28, 29, 44 and 45 were continuously monitored by MS. In another set of experiments, two consequent pulses of pure O_2 were introduced into the reactor after the CO_2 pulses (pulse #8 in above experiment) and after the H_2 pulses (pulse #14 in above experiment), and the evolution of ^{13}CO and $^{13}CO_2$ were monitored by the mass spectrometer to estimate the residual coke species on the catalyst after the CO_2/ H_2 pulses.

2.5. Kinetic Experiments

Preliminary experiments to investigate the presence of external and internal mass transfer limitations were conducted by varying the total flowrate and the catalyst particle size, as detailed

in the Supporting Information. The final kinetic measurements were conducted in the temperature range of 600-675°C and 1 bar pressure at a WHSV of 600 $Lg^{-1}h^{-1}$ on catalyst diluted with quartz silica in 1:3 ratio. Particle size of the catalyst was less than 100 μm. The feed gas containing CH_4, CO_2, CO and H_2 diluted in He was introduced at a total flowrate of 150 ml/min, and the partial pressure of the reactants were varied in the range of 3.4 to 26.7 kPa respectively. Reaction rates are presented in terms of turnover frequency. The forward rate of reaction is calculated as:

$$r_f = \frac{r_{CH_4}}{(1-\beta)} \qquad (11)$$

where r_{CH_4} is the rate of methane conversion calculated as per Eq. 7, and β is the approach to equilibrium $\beta = (\frac{{P_{H_2}}^2 {P_{CO}}^2}{K_{eq} P_{CH_4} P_{CO_2}})$.

Kinetic parameters were estimated by minimization of errors between the experimental data and the proposed kinetic model using a combination of Gauss–Newton and Levenberg–Marquardt methods using MATLAB software. Generic Algorithm method was used to create random initial guesses for each kinetic parameter.

3. RESULTS & DISCUSSION

3.1. Fresh Catalyst Characterization

3.1.1. Characterization of Ni-Phyllosilicate Core

A nickel phyllosilicate precursor was used to load and disperse Ni on silica nanospheres in the core of the Ni-PS@$Ce_{1-x}Zr_xO_2$ catalysts. A thin layer of Ni phyllosilicate on Stöber silica nanospheres was synthesized by the ammonia evaporation method, using silica nanospheres as

the support and silica-source for phyllosilicate formation [22]. TEM images of the Ni-PS core nanoparticles after drying (Figure S1a) exhibit sheet-like lamellar structures characteristic of phyllosilicates assembled on the silica nanosphere. It is noted from the TEM images (Figure S1) that only the external surface of the silica substrate is converted to phyllosilicate, which upon reduction decomposes to form well-dispersed Ni nanoparticles supported on a solid silica sphere (refer Scheme S1 for the schematic of the catalyst morphology). XRD pattern of the fresh Ni-PS core (Figure S2a) shows diffraction peaks at 2θ = 34, 37 and 61°, corresponding to the [200], [202] and [060] diffractions of pecoraite $Ni_3Si_2O_5(OH)_4$, respectively [23]. The formation of phyllosilicates is further confirmed from the FT-IR spectrum of the calcined Ni-PS sample (Figure S2b) from the characteristic bands at 1024, 670 and 710 cm^{-1} (refer SI for details) [24]. Further detailed characterization of the Ni-PS core can be found in our previous study [6].

3.1.2. Morphology of Core-shell Ni-PS@$Ce_{1-x}Zr_xO_2$ Catalysts

The morphology of the reduced Ni-PS@$Ce_{1-x}Zr_xO_2$ catalysts was observed by HRTEM.

The HRTEM images (Figure 1) show a thin outer layer of heavier material on the spherical Ni-PS core, that can be attributed to the $Ce_{1-x}Zr_xO_2$ shell. A uniform coating of the shell is observed for all the Ni-PS@$Ce_{1-x}Zr_xO_2$ samples (z = 0 – 0.2), with no exposed branches of the Ni-phyllosilicate sheets. A representative HRTEM image of the fresh Ni-PS@$Ce_{0.9}Zr_{0.1}O_2$ sample before reduction is presented in Figure S3a.

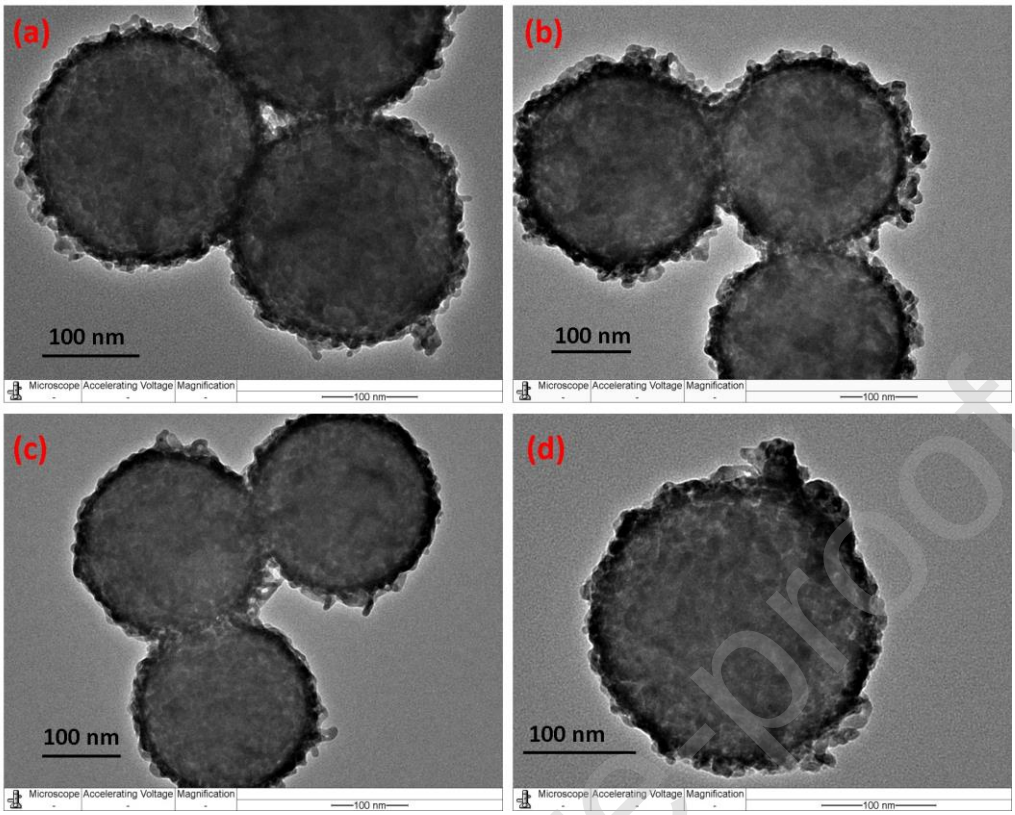

Figure 1. HRTEM images of reduced Ni-PS@$Ce_{1-x}Zr_xO_2$ catalysts (a) x = 0, (b) x = 0.05, (c) x = 0.1, (d) x = 0.2

The core-shell structure was confirmed from elemental mapping using TEM-EDX (Figure 2, Figure S4-S6). In Figure 2, the sandwiched core-shell structure of Ni-PS@$Ce_{0.9}Zr_{0.1}O_2$ can be observed from the relative intensities of the elements, wherein nickel is dispersed on the surface of silica nanospheres and is further coated by a thin shell containing Ce and Zr. Some of the Ni nanoparticles are also expected be embedded inside the ceria-zirconia shell because of protruding branches of the Ni-phyllosilicate carrier. A schematic for the sandwich core-shell structure is presented in Scheme S1. Signals for Ce and Zr are observed to overlap in the same region, reflecting the successful incorporation of Zr inside the cerium oxide shell. Zr loading was not increased beyond x = 0.2, because of non-uniform formation of the ceria-zirconia shell at higher Zr loading, as discussed in SI.

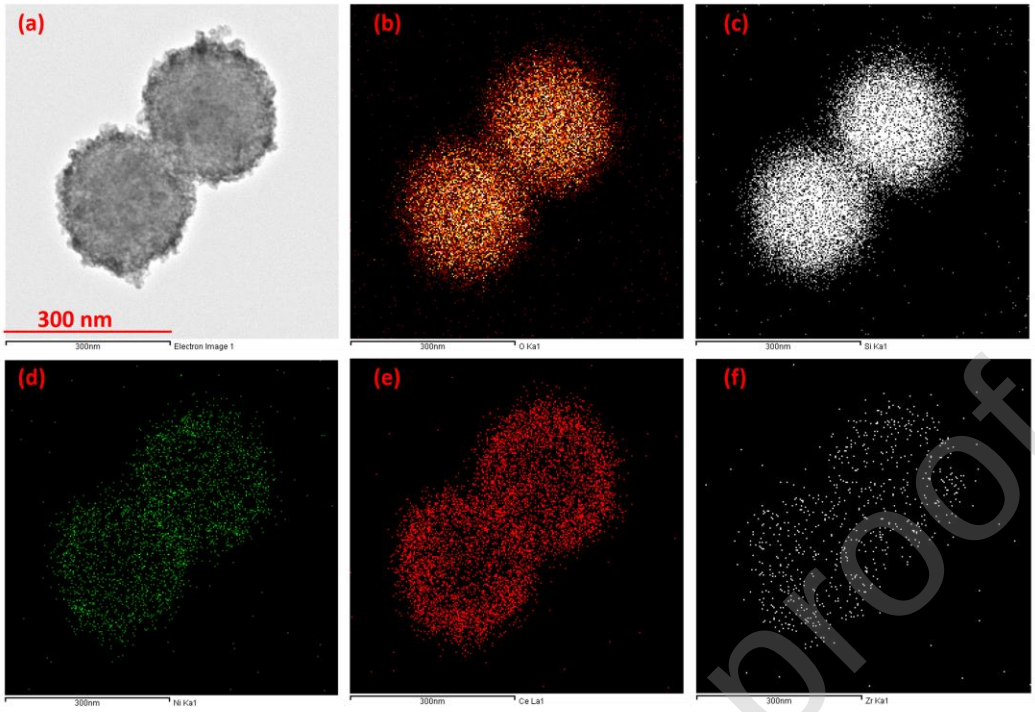

Figure 2. TEM-EDX elemental mapping of fresh Ni-PS@$Ce_{0.9}Zr_{0.1}O_2$ catalyst (a) TEM image, (b-f) elemental mapping of O, Si, Ni, Ce and Zr respectively for image (a).

HRTEM imaging of the reduced Ni-PS@$Ce_{1-x}Zr_xO_2$ catalysts at higher magnifications at locations near the inner edge of the ceria-zirconia shell reveal lattice fringes for Ni and ceria-zirconia support respectively (Figure S7). Nearly similar Ni particle size in the range of 3 – 5 nm is observed across all the catalysts (Figure S8, Table 1). Some studies on supported Ni/Ce-ZrO_2 catalysts have reported that Ni dispersion is influenced by the Zr loading [16, 25]; however, it appears that for a core shell structure, the Ni particle size is primarily determined by the segregation and encapsulation provided by the core-shell morphology and does not depend strongly on the Zr loading.

Table 1. Ni particle size and dispersion in reduced catalysts.

Catalyst	Ni particle size[a], nm	CO chemisorbed per gram Ni (μmol g_{Ni}^{-1})[b]	Surface Ni/ bulk Ni[c] (%)

Ni-PS@CeO_2	4.0 ± 0.8	211	1.2
Ni-PS@$Ce_{0.95}Zr_{0.05}$	3.8 ± 0.6	115	0.7
Ni-PS@$Ce_{0.9}Zr_{0.1}$	3.7 ± 0.4	106	0.7
Ni-PS@$Ce_{0.8}Zr_{0.2}$	3.9 ± 0.5	183	1.1

[a] measured by HRTEM of reduced catalyst.

[b] calculated by subtracting CO uptake on corresponding SiO_2@$Ce_{1-x}Zr_xO_2$ supports from that on Ni-PS @$Ce_{1-x}Zr_xO_2$ in CO pulse chemisorption experiments.

[c] measured from CO chemisorption quantity.

The textural properties of the reduced catalysts were measured by N_2 adsorption-desorption isotherms. The BET surface area of the reduced Ni-PS@$Ce_{1-x}Zr_xO_2$ catalysts are in the range of 26-34 m^2/g (Table S1). The relatively low overall specific surface area of the reduced core-shell catalyst is because of the largely non-porous Stöber silica core [6]. In contrast to previous reports on supported ceria-zirconia based catalysts [14], we do not observe a monotonic increase in BET surface area or textural stability with increasing Zr loading, possibly because the textural stability of these core-shell catalysts are primarily determined by the thermally stable silica core.

3.1.3. Elemental Composition

The actual composition of the synthesized catalysts was measured using ICP-OES and are reported in Table 2. The Ni content is observed to be similar in all catalysts, and a progressive incorporation of Zr is observed with a concurrent reduction in Ce content from Ni-PS@CeO_2 to Ni-PS@$Ce_{0.8}Zr_{0.2}O_2$. The actual Zr/Ce ratio is observed to be slightly lower than the nominal value used during synthesis, indicating that some loss of Zr occurred during washing and recovery of the synthesized catalyst. Nonetheless, the actual Zr/Ce ratio increases monotonically with the nominal Zr loading and the trends in physicochemical properties and catalytic activity may be attributed to the change in Zr/Ce content in the catalysts.

Table 2. Elemental composition of the fresh catalysts as determined by ICP-OES.

Catalyst	Ni, %	Ce, %	Zr, %	Ni + Ce + Zr, %	Zr/(Ce+Zr) %, ICP	Zr/(Ce+Zr) %, nominal
Ni-PS@CeO_2	3.81	21.03	0	24.85	0	0
Ni-PS@$Ce_{0.95}Zr_{0.05}$	3.32	20.61	0.92	24.85	4.25	5
Ni-PS@$Ce_{0.9}Zr_{0.1}$	3.47	19.68	1.68	24.82	7.85	10
Ni-PS@$Ce_{0.8}Zr_{0.2}$	3.47	17.73	2.88	24.09	13.96	20

3.1.4. Crystal Structure

Figure 3 shows the XRD pattern of the fresh Ni-PS@$Ce_{1-x}Zr_xO_2$ catalysts. Diffraction peaks corresponding to the cubic fluorite phase of ceria are observed for all catalysts at 2θ = 28.6, 33.1, 47.5, 56.4, 59.4, 69.6 and 76.7°, along with a weak peak at 61° for the nickel phyllosilicate phase in the catalyst core. An upshift in 2θ for the diffraction peaks of the ceria fluorite structure is observed upon the introduction of Zr in the catalyst, indicating a contraction in the cubic ceria lattice (Figure 3b). This lattice contraction is caused by the incorporation of Zr^{4+} with smaller ionic radius (0.72 Å) than Ce^{4+} (0.87 Å) in the CeO_2 lattice and indicates the formation of a ceria-zirconia solid solution [26]. Lattice parameters for the $Ce_{1-x}Zr_xO_2$ solid solution phase are estimated using Rietveld method (Table 3) and are in good agreement with Vegard's law.

The XRD pattern for Ni-PS@$Ce_{0.8}Zr_{0.2}O_2$ (x = 0.2) catalyst shows a small additional peak at 2θ = 32°, which can be attributed to the presence of monoclinic zirconia phase [27]. It is also noted that the calculated value of the cell parameter *a* for the ceria-zirconia solid solution phase does not decrease further when Zr loading is increased from x = 0.1 to 0.2. This shows that a pure

ceria-zirconia solid solution is formed only for lower Zr contents (x = 0.05, 0.1) and further Zr addition forms a separate ZrO_2 phase along with the ceria-zirconia solid solution.

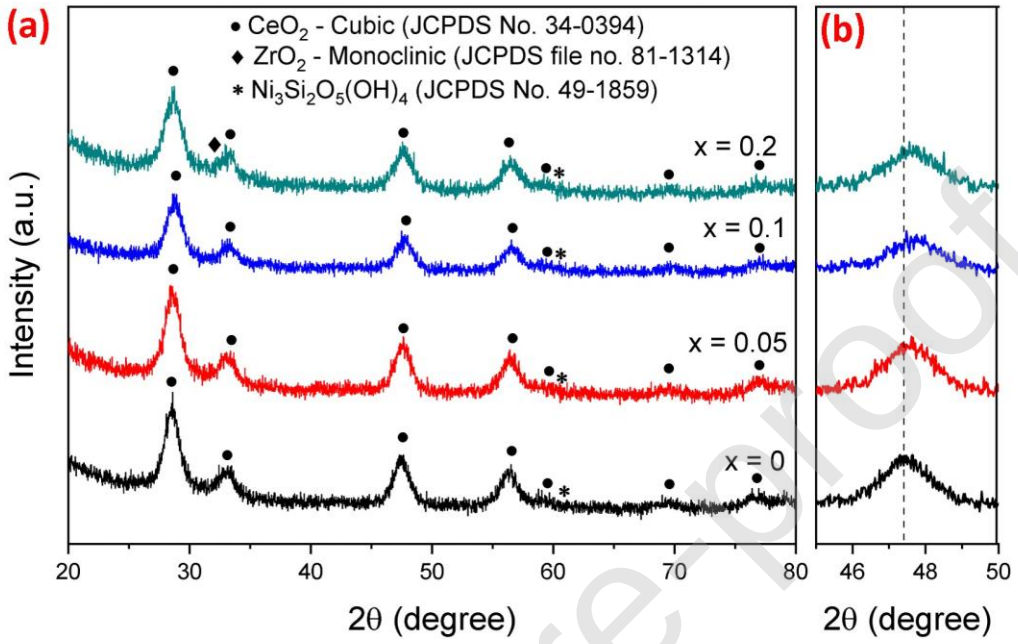

Figure 3. (a) Powder XRD pattern of calcined Ni-PS@$Ce_{1-x}Zr_xO_2$ samples (x = 0 to 0.2), (b) corresponding XRD pattern in 2θ range of 45 – 50° showing the shift in diffraction peak for [220] plane of ceria cubic lattice.

The XRD patterns for reduced Ni-PS@$Ce_{1-x}Zr_xO_2$ catalysts (Figure S9) show an attenuation of intensity of all the observed peaks for ceria-zirconia, which is likely caused by the formation of lattice defects (oxygen vacancies) by the reduction treatment, that breaks the long-range symmetry of the crystals [28]. HRTEM images of the reduced catalysts (Figure S7) show characteristic lattice fringes for fluorite CeO_2, indicating that it is still crystalline after reduction. XRD peaks for metallic Ni are not observed in the reduced catalysts, indicating that Ni crystal size is too small to be detected by XRD. The absence of Ni XRD peaks may also be caused by the low Ni content and the scattering of X-rays by cerium oxide.

Table 3. Cell parameters, oxygen storage capacity and Ce 3d XPS parameters of reduced catalysts.

Catalyst	Lattice parameter of $Ce_{1-x}Zr_xO_2$ shell, *a* (Å)		Oxygen Storage Capacity [b], µmol g^{-1}	$Ce^{3+}/(Ce^{3+} + Ce^{4+})$ after H_2 reduction [c]
	Calculated [a]	Vegard's Law		
Ni-PS@CeO_2	5.4149	5.4220	139	0.27
Ni-PS@$Ce_{0.95}Zr_{0.05}$	5.4029	5.4078	206	0.31
Ni-PS@$Ce_{0.9}Zr_{0.1}$	5.3905	5.3959	190	0.31
Ni-PS@$Ce_{0.8}Zr_{0.2}$	5.3962	5.3756	132	0.27

[a] Cell parameter is estimated by Rietveld refinement of powder XRD patterns.

[b] Calculated from amount of oxygen desorbed during O_2-TPD in the temperature range of 400-850ºC.

[c] Calculated from Ce 3d spectra of the reduced catalysts after reduction in pure H_2 at 750ºC for 1 h.

3.1.5. Reducibility

H_2-TPR was conducted to probe the reducibility of the catalysts (Figure 4). All the Ni-PS@$Ce_{1-x}Zr_xO_2$ catalysts are characterized by a complex reduction profile with multiple overlapping peaks from the reduction of Ni^{2+} and the partial reduction of Ce^{4+}. The peak at low temperature (below 300ºC) is assigned to the reduction of easily reducible oxygen species chemisorbed on oxygen vacancies formed by the replacement of Ce^{4+} with Ni^{2+} forming a solid solution [29].

The broad peak between 300ºC and 700ºC can be assigned to the reduction of Ni^{2+} species in the phyllosilicate structure to Ni^0 and of surface Ce^{4+} to Ce^{3+}. Reduction of Ni^{2+} in the Ni-phyllosilicate structure occurs in the temperature range of 450 – 750ºC [6]. The coating of ceria-zirconia on the Ni-PS core results in nickel species with varying degrees of interaction with silica and ceria-zirconia, which may result in multiple reduction peaks at different temperatures.

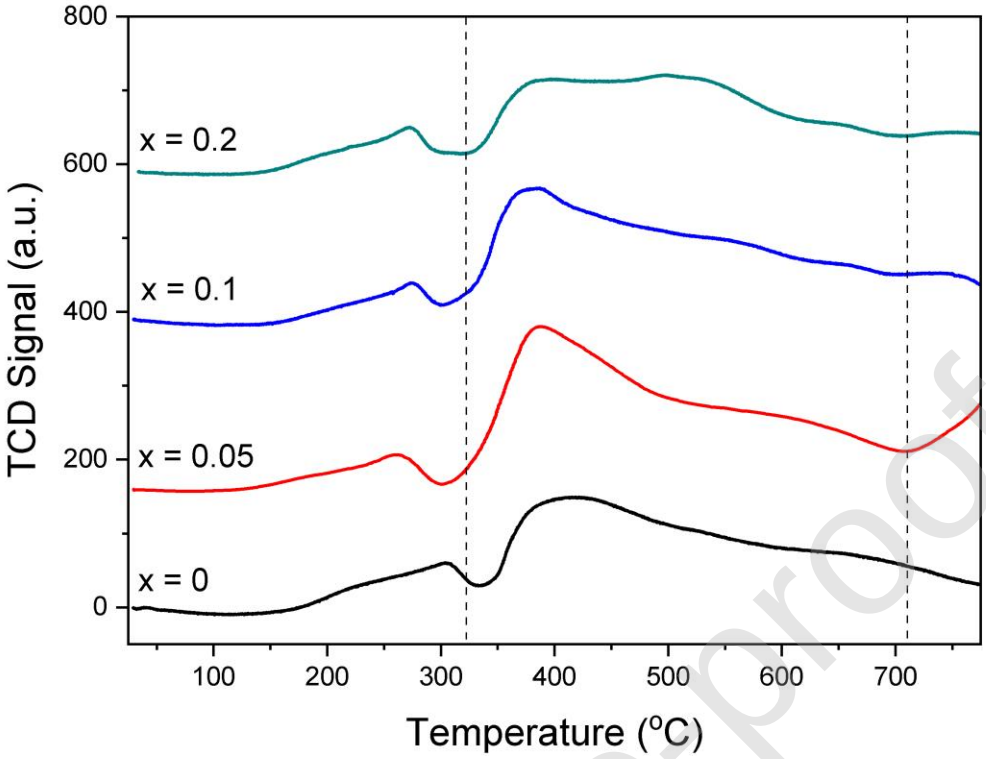

Figure 4. H_2-TPR profile of Ni-PS@$Ce_{1-x}Zr_xO_2$ samples (x = 0 to 0.2)

A significant contribution from the surface reduction of Ce^{4+} to Ce^{3+} to the observed reduction peak between 300°C and 700°C is inferred from the quantification of H_2 consumption in TPR (Table S2). The hydrogen consumption in the temperature range of 300°C and 700°C corresponds to 235 - 310 % of the stoichiometric hydrogen requirement to completely reduce all the Ni^{2+} to Ni^0, and the excess H_2 consumption can be attributed to Ce^{4+} surface reduction. The moles of H_2 consumed per mole Ni is much higher for the catalysts with Zr fraction of x = 0.05 and 0.1 (300-310 %) than the other catalysts (235-245%) as shown in Table S2, implying that the reducibility of Ni and ceria increases upon doping small amounts of Zr. The temperatures of the reduction peaks are also shifted to lower temperatures for x = 0.05 and 0.1. The improvement of reducibility of ceria upon the partial substitution of Ce^{4+} by Zr^{4+} in the fluorite structure is well-accepted in literature [14, 16, 30].

When the Zr loading was further increased to x = 0.2, a drop in the hydrogen consumption in TPR was observed. The decrease in overall reducibility can be attributed to the higher fraction of Zr^{4+} and the formation of a separate monoclinic ZrO_2 phase that is not reducible at these temperatures [16]. Compared to the other catalysts (x = 0 to 0.1), a more prominent peak in the higher temperature range of 500 – 600°C is observed for Ni-PS@$Ce_{0.8}Zr_{0.2}O_2$, whereas the peak between 300 – 500°C is reduced in intensity. Ni K-edge XANES analysis of the reduced catalysts (discussed in Section 3.1.6.) suggests that the peak at 500 – 600°C is related to nickel reduction. This indicates that high Zr loading and the presence of a ZrO_2 phase in Ni-PS@$Ce_{0.8}Zr_{0.2}O_2$ also decreases the reducibility of Ni in the catalyst, possibly by creating nickel species with strong interaction with ZrO_2 phase in the shell.

3.1.6. Chemical State of Ni

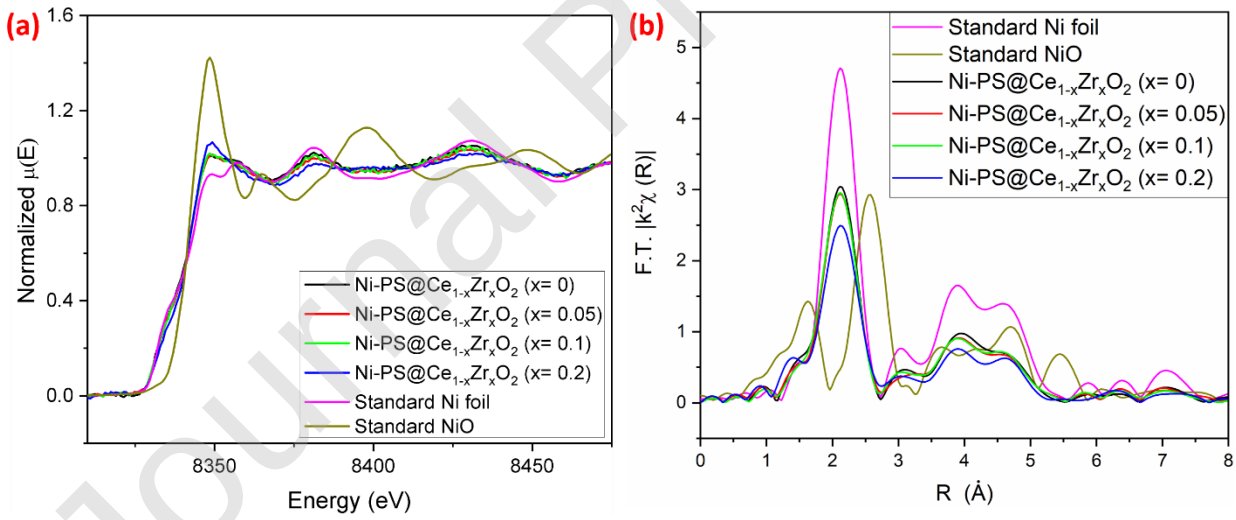

Figure 5. (a) Ni K-edge XANES spectra and (b) Fourier transform of Ni K-edge EXAFS spectra for reduced Ni-PS@$Ce_{1-x}Zr_xO_2$ (x = 0 to 0.2) catalysts and standard Ni foil and NiO.

The chemical state and local coordination environment of Ni in the reduced catalysts after H_2 reduction at 750°C was investigated using X-ray absorption spectroscopy (Figure 5). The

XANES spectra for the reduced Ni-PS@$Ce_{1-x}Zr_xO_2$ catalysts with x = 0, 0.05 and 0.1 closely resemble that of metallic Ni foil with no white line intensity and an absorption edge at approximately 8332 eV (Figure 5a). This shows that Ni is completely reduced to metallic state after H_2 reduction at 750^{o}C for these catalysts. In comparison, the XANES spectrum for the reduced Ni-PS@$Ce_{0.8}Zr_{0.2}O_2$ catalyst shows a small white line intensity, indicating that part of the Ni exists as Ni^{2+} (approximately 25% Ni^{2+} estimated by a linear combination fitting of the XANES spectra using Ni and NiO standards). The lower degree of reduction of Ni in Ni-PS@$Ce_{0.8}Zr_{0.2}O_2$ agrees well with the H_2-TPR results.

The local coordination structure of Ni in the reduced Ni-PS@$Ce_{1-x}Zr_xO_2$ catalysts was estimated from EXAFS analysis at the Ni K-edge (Figure 5b). In the R range of 1-3 Å, the FT-EXAFS spectra of Ni-PS@$Ce_{1-x}Zr_xO_2$ for x = 0 to 0.1 show one peak around R = 2.1 Å, corresponding to the first Ni-Ni coordination shell in metallic Ni with a face centered cubic structure. In addition to this, the reduced $Ce_{0.8}Zr_{0.2}O_2$ (x = 0.2) sample shows an additional contribution from Ni-O coordination around R = 1.6 Å, because of incomplete reduction of Ni. The fitting of the FT-EXAFS spectra is shown in Table S3 and Figure S10, respectively. The fitted coordination number (C.N.) of Ni-Ni coordination shell is lower than the ideal value of 12 in Ni foil because of the finite size of the nickel nanoparticles in the catalysts. The Ni-Ni coordination number is observed to be similar for Zr nominal loading x = 0 to 0.1 and is lower for x = 0.2, which is because EXAFS is a bulk characterization technique and part of the Ni exists in oxidized state in Ni-PS@$Ce_{0.8}Zr_{0.2}O_2$. The similarity in the values of the Ni-Ni C.N. for all the catalysts indicates similar Ni particle size irrespective of Zr doping level, which agrees with HRTEM observations.

3.1.7. Oxygen Storage Capacity

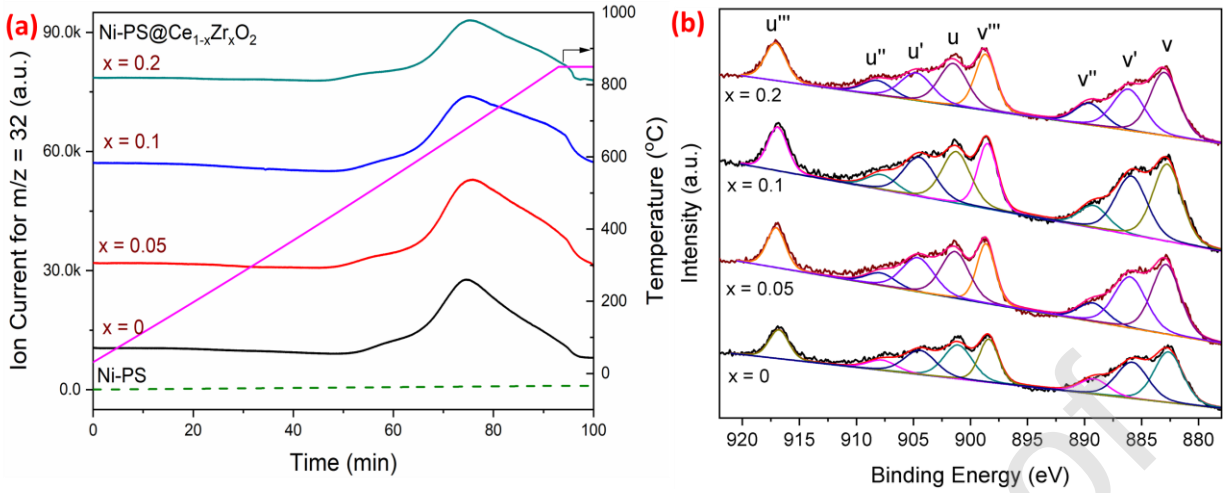

Figure 6. (a) Mass spectra for O_2-TPD of Ni-PS@$Ce_{1-x}Zr_xO_2$ (x = 0 to 0.2) catalysts and Ni-PS core (reference), (b) Ce 3d XPS spectra of reduced Ni-PS@$Ce_{1-x}Zr_xO_2$ (x = 0 to 0.2) catalysts.

The oxygen storage/release capacity of the reduced Ni-PS@$Ce_{1-x}Zr_xO_2$ catalysts were investigated using temperature programmed desorption of O_2 under He flow. The active oxygen species desorbed from ceria-zirconia can usually be divided into three types: (1) O_α species, desorbed at <350°C corresponding to chemically adsorbed oxygen species (O_2^-/ O^-/ O_2^{2-}) with weak adsorption on the ceria-zirconia surface, (2) O_γ species desorbed above 700°C, assigned to oxygen in the crystal lattice and (3) O_β species, desorbed between 350°C to 700°C, related to oxygen species chemically adsorbed on oxygen vacancy sites and partial lattice oxygen [31-33].

O_2-TPD results (Figure 6a) show the release of O_β and O_γ species from the lattice of all the Ni-PS@$Ce_{1-x}Zr_xO_2$ catalysts. O_2 desorption during the TPD experiment can be assigned only to the ceria-zirconia lattice oxygen because no desorption is observed in a control experiment with just the Ni-PS core. The amount of oxygen desorbed from the ceria shell increases significantly when Zr is added at x = 0.05 and 0.1, with Ni-PS@$Ce_{0.95}Zr_{0.05}O_2$ showing the highest oxygen storage capacity, closely followed by Ni-PS@$Ce_{0.9}Zr_{0.1}O_2$ (Table 3). The distortion of the ceria lattice by the insertion of Zr^{4+} causes weakening of the Ce-O bond and an increased reducibility of Ce^{4+} to Ce^{3+}, facilitating the formation of oxygen vacancies and the release of lattice oxygen [13, 14, 30,

34]. However, further increasing the Zr doping to x = 0.2 resulted in a reduction of the amount of O_2 desorption in the TPD, possibly because of its lower reducibility and the formation of a separate zirconia phase, which does not participate in the redox process and may hinder the transport of lattice oxygen [25].

The change in the oxygen storage/transport properties of the catalysts with various Zr loadings was also confirmed by Ce 3d XPS analysis of the reduced samples. The ratio of Ce^{3+} to the total Ce (Ce^{3+} + Ce^{4+}) in the catalyst after H_2-reduction is a good indicator of the amount of lattice oxygen that is desorbed during redox cycling, where a higher fraction of Ce^{3+} implies a higher amount of oxygen released [34, 35]. It is noted that the reduced samples were briefly exposed to air while transferring to XPS chamber, which may lead to some surface oxidation; however significant oxidation of Ce^{3+} is not expected for short exposure to air at room temperature [33]. The Ce 3d XPS spectra for reduced Ni-PS@$Ce_{1-x}Zr_xO_2$ catalysts (Figure 6b) can be deconvoluted into eight peaks assigned to Ce $3d_{5/2}$ (v) and Ce $3d_{3/2}$ (u) contributions. The v, v", v"' and u, u", u"' bands belong to Ce^{4+} ions, and the v' and u' bands belong to Ce^{3+} ions [35]. The Ce^{3+}/ (Ce^{3+} + Ce^{4+}) fraction in the surface lattice of the reduced Ni-PS@$Ce_{1-x}Zr_xO_2$ increases at Zr doping of x = 0.05 and 0.1 compared to the Ni-PS@CeO_2 catalyst (Table 3). Further increase in Zr loading to x = 0.2 results in a drop in the Ce^{3+} fraction. These results are completely in agreement with the O_2-TPD results.

3.1.8. CO Pulse Chemisorption and SMSI Effect

Pulse chemisorption with CO as a molecular probe was used to measure the exposed nickel surface area in the reduced catalysts. The amount of CO chemisorbed on Ni was calculated by subtracting the contribution of ceria-zirconia (CO uptake on corresponding SiO_2@$Ce_{1-x}Zr_xO_2$

from that on the Ni-PS@$Ce_{1-x}Zr_xO_2$ catalysts). Relatively low CO uptake on Ni was observed on all the reduced Ni-PS@$Ce_{1-x}Zr_xO_2$ catalysts, with the adsorbed CO/total Ni content in the range of 0.7 – 1.2% on a molar basis. For reference, the measured CO uptake on the reduced Ni-PS core corresponds to 4.9% of bulk Ni. The much lower CO uptake on the core-shell catalysts compared to the Ni-PS core can be caused primarily by a combination of two factors: 1. the core-shell structure, where the ceria-zirconia crystals are deposited on the Ni, thereby blocking a significant portion of the exposed Ni atoms, 2. the occurrence of strong metal-support interaction (SMSI) between Ni and ceria-zirconia induced by high temperature reduction. The suppression of chemisorption capacity of CO or H_2 on group VIII metals by the SMSI effect on easily reducible supports like CeO_2 or TiO_2 have been well documented in literature [36, 37]. In a reducing atmosphere at elevated temperatures, lattice expansion by partial reduction of Ce^{4+} to Ce^{3+} induces the migration of ceria to the surface of the metal nanoparticles and leads to surface decoration or partial encapsulation of the metal nanoparticles [36, 38], which can suppress the chemisorption capacity of the metal.

The relative amount of CO chemisorbed on the reduced Ni-PS@$Ce_{1-x}Zr_xO_2$ catalyst follows the inverse trend of the reducibility of the ceria-zirconia shell, with lower CO chemisorption on catalysts with x = 0.05 and 0.1 (Table 1). The increased reducibility of ceria upon Zr doping may be expected to result in higher Ni encapsulation and stronger MSI in these two catalysts. The lower CO chemisorption on these catalysts (x = 0.05 and 0.1) is thus attributed to an increase in SMSI effect and higher interaction/interface formation of Ni with shell. Both Ni-PS@CeO_2 and Ni-PS@$Ce_{0.8}Zr_{0.2}O_2$ show lower Ni encapsulation and higher CO chemisorption capacity.

3.2. Catalyst activity and coke-resistance in DRM

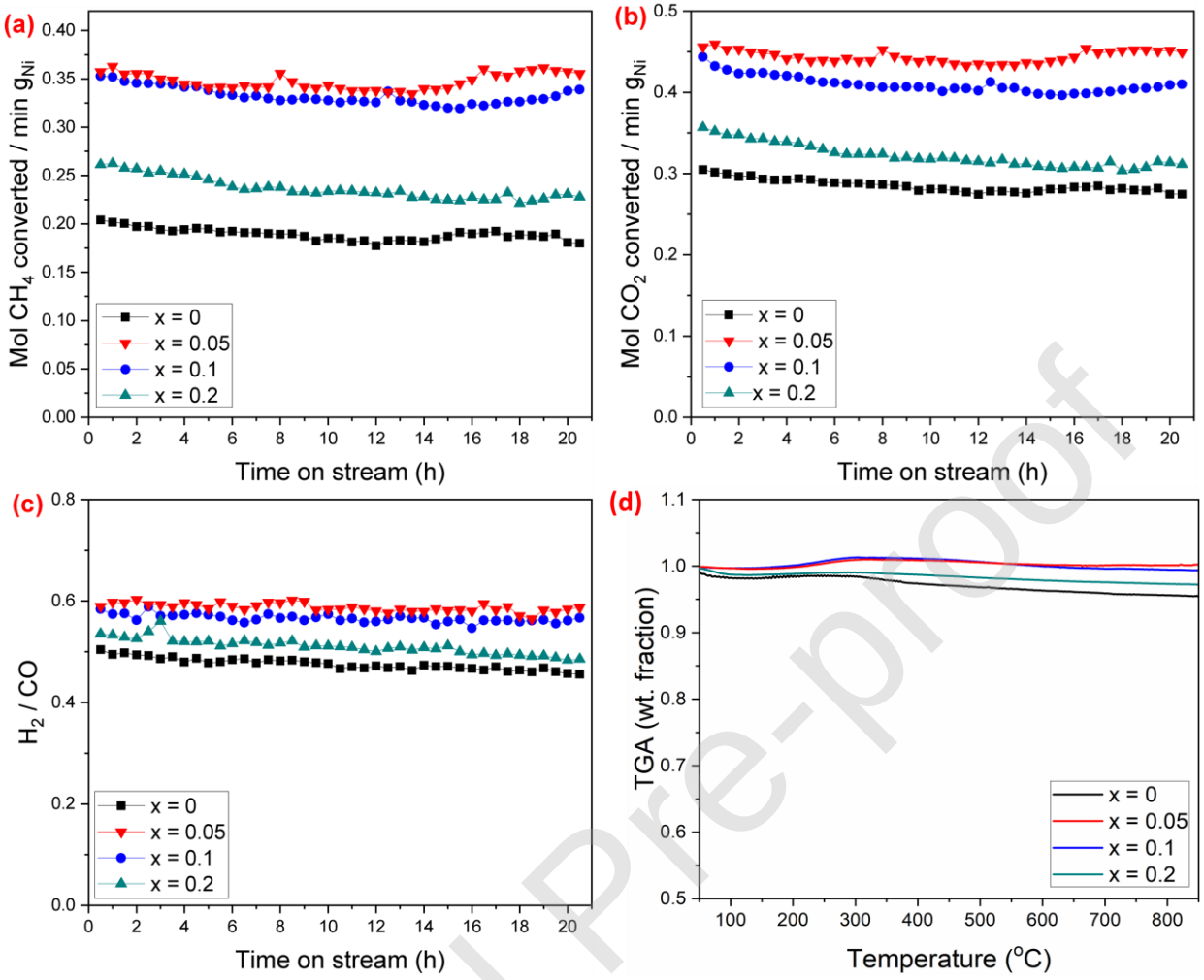

Figure 7. (a-c) DRM activity on the Ni-PS@$Ce_{1-x}Zr_xO_2$ catalysts at 600°C, 1 bar, WHSV = 200 $Lh^{-1}g^{-1}$ and CH_4/ CO_2 = 1/1 - (a) CH_4 conversion activity, (b) CO_2 conversion activity, (c) H_2/CO ratio; (d) TGA-DTA of spent catalysts after 20 h DRM.

The DRM activity of the Ni-PS@$Ce_{1-x}Zr_xO_2$ catalysts was tested at 600°C for 20 h with an un-diluted feed of equimolar CH_4 and CO_2. A high WHSV of 200 $Lh^{-1}g^{-1}$ was maintained to keep the reactant conversions below 25% and probe the intrinsic activity of the catalysts. Mear's number MR and Weisz-Prater parameter C_{WP} (Eq. S1, S2) were estimated to be 0.008 and 0.013, respectively at these conditions, which are much lower than the threshold values of 1.5 and 1, respectively, above which external and internal mass transfer limitations become dominant.

It is observed that Ni-PS@$Ce_{1-x}Zr_xO_2$ catalysts with Zr loadings of x = 0.05 and 0.1 demonstrated approximately 1.75 times the specific CH_4 conversion activity (per g_{Ni}) and 3.4 times higher turnover frequency (TOF) compared to Ni-PS@CeO_2. Further increase in Zr fraction to x = 0.2 leads to reduction of activity. Thus, there is an optimum composition of the ceria-zirconia shell that leads to a maximum improvement in DRM activity (Figure 7a,b).

The observed effect of the Zr loading on the DRM activity in these core-shell catalysts agree well with some previous investigations of ceria-zirconia supported metal catalysts. For example, Zhang et al. [16] reported 1.5 times methane conversion on Ni/$Ce_{0.8}Zr_{0.2}O_2$ than on Ni/CeO_2. Makri et al. [19] reported a significant drop in conversion when the Zr fraction in Ni/$Ce_{1-x}Zr_xO_2$ was increased from 0.2 to 0.5. Thus, we observe that the trend in DRM activity with the Zr content remains similar for both supported catalysts and core-shell catalysts.

The initial TOF for CH_4 conversion, calculated by normalizing the specific activity by the moles of surface exposed Ni atoms, increased in the order of Ni-PS@CeO_2 (16 s^{-1}) < Ni-PS@$Ce_{0.8}Zr_{0.2}O_2$ (23 s^{-1}) < Ni-PS@$Ce_{0.95}Zr_{0.05}O_2$ (51 s^{-1}) ≈ Ni-PS@$Ce_{0.9}Zr_{0.1}O_2$ (55 s^{-1}) (Figure S11). It is interesting to observe that the calculated TOF on the catalysts has a negative correlation with the exposed Ni surface area; both the specific activity and TOF are higher on the catalysts which have lower Ni surface area (x = 0.05 and 0.1). It may however be noted that calculating TOF based on the number of exposed Ni atoms may not always provide an accurate representation of the true activity of such bi-functional catalysts. In such catalysts, where the support (ceria-zirconia in this case) is also involved in the reaction, the key elementary steps of the reaction may occur on the metal-support interface rather than the exposed metal surface, as we discuss in further detail in Section 3.3 [39]. Unfortunately, it is extremely difficult to correctly estimate the Ni/$Ce_{1-x}Zr_xO_2$ interface area for these core-shell catalysts where the metal-

support perimeter cannot be easily defined [40]. Qualitatively, we observe that the catalysts with more SMSI effect and consequently, more Ni/support interface, display higher DRM activity, which may indicate that Ni/$Ce_{1-x}Zr_xO_2$ is the active site for the kinetically relevant reaction steps.

The specific activity per gram Ni of the Ni-PS@$Ce_{1-x}Zr_xO_2$ is compared with those of representative Ni catalysts reported in the recent years for DRM (Table S4). The core-shell Ni-PS@$Ce_{0.9}Zr_{0.1}O_2$ catalyst presents one of the highest specific activities reported for DRM. The high specific activity of the core-shell Ni-PS@$Ce_{0.9}Zr_{0.1}O_2$ catalyst despite the significantly low Ni surface exposure in the core-shell catalyst is an indication of the promotional effect of the higher metal-support interface on the catalyst activity.

The spent catalysts after the DRM activity test at 600^{o}C for 20 h were examined by TGA and HRTEM to analyze the coke deposition during the reaction (Figure 7d). Negligible weight loss (<1 wt%) is observed for all the spent catalysts in TGA, indicating almost no coke residue. This demonstrates the excellent coke-resistance of these catalysts, attributed primarily to the core-shell morphology. The formation of filamentous carbon is largely suppressed because of the encapsulation effect of the ceria-zirconia shell. The absence of coke is also verified from the HRTEM images of the spent catalysts (Figure S12).

Long-term stability was also demonstrated on the Ni-PS@$Ce_{0.9}Zr_{0.1}O_2$ catalyst for 96 h at both 600^{o}C and 800^{o}C (Figure S13). Spent catalyst characterization after the stability test for 96 h show very low coke formation (Figure S14). Comparison with reported supported Ni catalysts (Table S5) shows the distinct superiority of these core-shell Ni-PS@$Ce_{1-x}Zr_xO_2$ catalysts in terms of coke-resistance.

Thus, overall, we observe that the DRM activity of the core-shell catalyst is enhanced substantially by the doping of a small amount of Zr in the shell, and the catalysts exhibit excellent stability and resistance to coke deposition under extended testing in DRM. The increase in activity with Zr doping shows a positive correlation with the oxygen storage capacity and oxygen mobility of the $Ce_{1-x}Zr_xO_2$ shell. Previous investigations on conventional supported catalysts with metal nanoparticles (Ni, Pt, Rh etc.) dispersed on ceria-zirconia supports have inferred several possible reasons for the improvement in DRM activity by Zr doping such as: suppression of Ni sintering during reduction/reaction, improvement in thermal stability of ceria support, increase in reducibility of Ni, increase in support OSC, suppression of migration of Ni ions into the ceria lattice forming $Ni_yCe_{1-y}O_{2-ö}$ solid solution, and reduction in surface-blocking coke deposits [14, 16, 26, 27, 41, 42]. Clearly, several aspects of the physical and chemical properties of the catalyst are simultaneously changed by doping Zr, which results in a complex dependence and often contradictory observations on the catalyst performance in literature.

The core-shell morphology of our catalyst allows us to decouple some of these factors and attempt a simpler and more insightful analysis of the effect of Zr doping, by keeping some of these aspects unchanged over all the catalysts. In the core-shell Ni-PS@$Ce_{1-x}Zr_xO_2$ catalysts, the particle size of Ni and its growth during reduction/reaction is observed to be quite independent of the Zr doping, in contrast with supported catalysts, where the difference in thermal stability of ceria and zirconia can significantly affect metal sintering. Very little Ni sintering was observed in the spent catalysts after reaction at 600^{o}C by HRTEM (Figure S15, S16), because of the protection of the sandwiched core-shell structure against particle migration and coalescence. Similarly, a significant effect of the thermal stability of zirconia vs. ceria on the overall DRM activity on these core-shell catalysts may also be excluded based on the similarity of the BET

specific surface areas of the spent catalysts (Table S1). Finally, the effect of coke formation, which is often an important factor affecting the catalytic activity of supported Ni catalysts, may also be neglected in our case, since coke formation is negligible in all these core-shell catalysts.

Considering the above effects, we infer that the enhancement in DRM activity by a small amount of Zr doping in the Ni-PS@$Ce_{1-x}Zr_xO_2$ catalysts can be attributed primarily to two factors: 1. the increase in oxygen mobility and OSC of the ceria-zirconia shell, and 2. increase in SMSI effect of ceria-zirconia on Ni, that likely leads to higher Ni/ceria-zirconia interface area. In the following section, we attempt to rationalize this positive effect of the lattice oxygen mobility and storage capacity on the DRM reaction rate from a mechanistic and kinetic aspect.

3.3. Kinetic and Mechanism Study

Increase in oxygen storage/ transport capacity of the support has frequently been reported in literature as one of the factors increasing DRM activity [43]; however, exactly how this factor affects the kinetics of the DRM reaction has not been clearly established. While the role of the lattice oxygen of ceria in scavenging surface-bound carbon is quite well accepted [11, 19], this does not necessarily explain a higher overall reaction rate, because this carbon-oxidation step may not necessarily be the rate determining step of DRM. So, here we attempt to correlate this observed dependence of DRM rates on the oxygen storage/ transport properties of ceria-zirconia through a mechanism and kinetic study on Ni-PS@$Ce_{0.9}Zr_{0.1}O_2$.

3.3.1. Kinetic Experiments

Suitable operating conditions for kinetic measurements were chosen where external and internal mass transfer limitations can be neglected. Details of these preliminary tests and results are provided in the Supporting Information (Figure S17).

3.3.1.1. Apparent Activation Energy

The activation energy of a reaction is a key parameter defining the activity of a catalyst. The effect of reaction temperature on the methane turnover frequency was measured on both the Ni-PS@CeO_2 and Ni-PS@$Ce_{0.9}Zr_{0.1}O_2$ catalysts in the temperature range of 600-675^{o}C. The Arrhenius plot is linear, indicating that the activation energy is constant over the measured temperature range (Figure 8a). The calculated value of activation energy (ΔE) for both the catalysts is in the range of reported activation energy for DRM on various Ni-based catalysts, which typically lies between 33–100 kJ mol^{-1} [44-46].

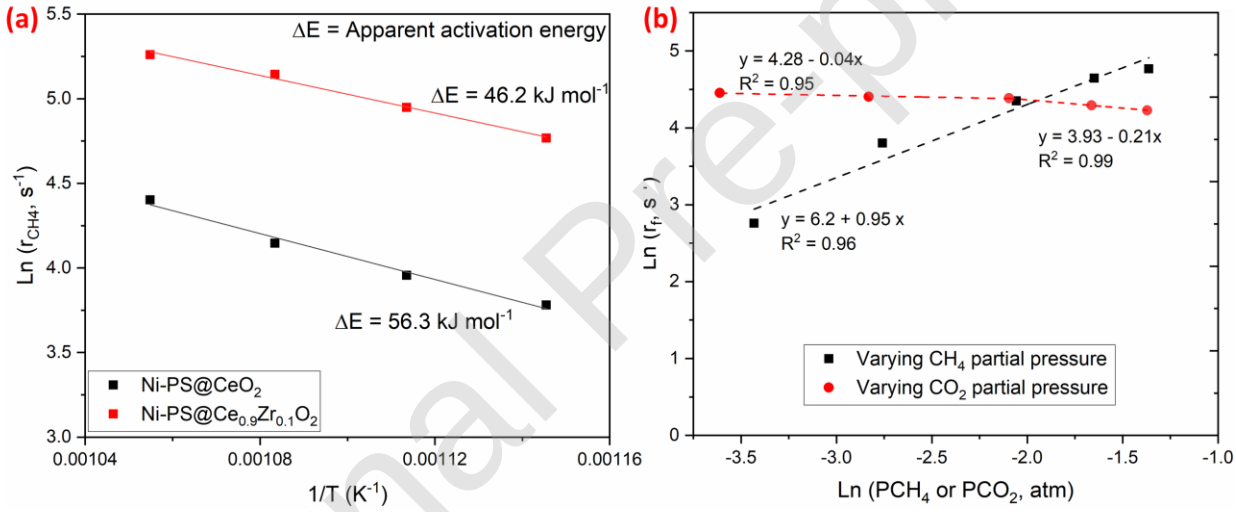

Figure 8. (a) Arrhenius plot of methane conversion rate on Ni-PS@CeO_2 and Ni-PS@$Ce_{0.9}Zr_{0.1}O_2$, (b) determination of power law kinetic rate model by varying partial pressures of CH_4 and CO_2 over Ni-PS@$Ce_{0.9}Zr_{0.1}O_2$ at 600°C.

It is observed that the apparent activation energy for CH_4 conversion in DRM is lower for Ni-PS@$Ce_{0.9}Zr_{0.1}O_2$ (46.2 kJ mol^{-1}) than on Ni-PS@CeO_2 (56.3 kJ mol^{-1}). It is hypothesized that the higher oxygen mobility of the Ni-PS@$Ce_{0.9}Zr_{0.1}O_2$ catalyst reduces the activation barrier of the rate determining step, which manifests in its higher DRM activity compared to Ni-PS@CeO_2.

3.3.1.2. Apparent Reaction Order

The apparent reaction orders of CH_4 and CO_2 for DRM on Ni-PS@$Ce_{0.9}Zr_{0.1}O_2$ were evaluated by studying the effect of the partial pressures of the reactants on the observed reaction rate and fitting the kinetic data to the power law (Eq. 12). The plots of the logarithm of the CH_4 forward reaction rate vs. the logarithm of CH_4 and CO_2 partial pressures at 600°C are shown in Figure 8b.

$$r_{CH_4} = A \exp\left(\frac{-E_a}{RT}\right) {P_{CH_4}}^m {P_{CO_2}}^n (1-\beta) \qquad (12)$$

where, $\beta = \left(\frac{{P_{H_2}}^2 {P_{CO}}^2}{K_{eq} P_{CH_4} P_{CO_2}}\right)$ and $K_{eq} = \exp(-(252.35 - 0.2659T - 1.1x10^{-5}T^2) * 10^3 / RT)$ [47]

The forward reaction rate was observed to increase monotonically with an increase in CH_4 partial pressure with an apparent reaction order close to 1 (m = 0.95). First order dependence of the forward reaction rate of DRM on methane partial pressure has been reported widely in literature on Ni catalysts and indicates that dissociation of C-H bond in CH_4 is a rate-limiting step [45-48]. A weak inhibition was observed at methane partial pressure over stoichiometric values, which may be associated with the formation of surface-blocking coke species.

A much weaker dependence of the reaction rate on the CO_2 partial pressure was observed, with an almost zero-order dependence (n = -0.04) on CO_2 for a CO_2 partial pressure up to stoichiometric equivalent of CH_4. The near-zero order dependence of the forward turnover rate on the CO_2 partial pressure indicates that CO_2 activation is kinetically insignificant for this catalyst [46, 49]. An inhibitory effect of CO_2 is observed (n = -0.21) when CO_2 is supplied in excess of CH_4. Such inhibitory effect by excess CO_2 on Ni catalysts has been reported in literature and is likely caused by surface oxidation of Ni in CO_2-rich atmosphere that causes a loss in activity [47].

3.3.2. Proposed Mechanism and Kinetic Model

A bi-functional Mars van Krevelen type mechanism is generally accepted in literature for methane reforming or partial oxidation on catalysts with redox supports such as ceria-zirconia [6, 20, 50]. In this mechanism, CH_x intermediate formed from the decomposition of methane is converted into CO by the lattice oxygen species of ceria generating oxygen vacancies. The gas-phase oxidant CO_2 then dissociates on these oxygen vacancies to produce CO and back-fill the vacancies.

The validity of this redox mechanism on the Ni-PS@$Ce_{1-x}Zr_xO_2$ catalyst was verified from the observation of oxygenated products (CO, CO_2) upon introducing CH_4 on the reduced catalysts. Both CO and CO_2 formation were observed in the transient response upon flowing CH_4 on the reduced catalysts, clearly showing the release and reaction of lattice oxygen from the ceria-zirconia shell (Figure S18). *In situ* DRIFTS experiments with alternate pulses of CH_4 and CO_2 on Ni-PS@$Ce_{0.9}Zr_{0.1}O_2$ also support the occurrence of the MvK redox mechanism (refer SI, Figure S19). Comparing between the transient responses of CH_4 exposure of Ni-PS@CeO_2 and Ni-PS@$Ce_{0.9}Zr_{0.1}O_2$ (Figure S18), it is observed that the amount of CO and CO_2 formed is higher on Ni-PS@$Ce_{0.9}Zr_{0.1}O_2$, reflecting its higher oxygen storage capacity. It is also interesting to note from the transient traces of CO and CO_2 that there is a shorter time delay between CH_4 introduction and CO/CO_2 formation on Ni-PS@$Ce_{0.9}Zr_{0.1}O_2$ than on Ni-PS@CeO_2. This may indicate faster kinetics of DRM and higher reactivity of lattice oxygen on the Zr-doped catalyst, as observed in the apparent activation energy measurements.

The analysis of apparent reaction orders of the reactants suggests that methane decomposition is the sole rate determining step on this catalyst, in agreement with several previous investigations

on reaction mechanism on Ni catalysts [51, 52]. In supported metal catalysts, methane decomposition is believed to occur primarily on metal sites, and the role of support lattice oxygen has been proposed to be in oxidizing CH_x species from methane dissociation [20].

Considering that methane decomposition is the rate determining step, the pronounced effect of the oxygen storage capacity of the $Ce_{1-x}Zr_xO_2$ shell on the DRM reaction rate seems counter-intuitive. However, the effect of the support on DRM activity has been reported ubiquitously in literature. Several investigations on Ni catalysts have concluded that the support can alter the activation energy of the reaction [53]. Bradford et al. showed that the that the specific activity for DRM depends on both the metal electronic structure and the support for partially reducible supports [54]. Specifically, the addition of redox promoters such as ceria on catalysts with non-reducible supports have often been reported in literature to enhance DRM activity [55]. This shows that even though the support may not be the direct site for methane adsorption and dissociation, it can influence the activation barrier for methane dissociation on the metal site.

To better explain the observed role of the support - specifically the redox properties and oxygen mobility – on the overall kinetics of DRM, we propose that the lattice oxygen of ceria-zirconia is involved not only in oxidation of carbonaceous intermediates, but also in activation of methane. Dissociation of C-H bond of methane on a metal site may occur by two main routes – 1. direct cleavage of C-H bonds to form $CH_x - *$ $(x = 3 - 0)$, 2. oxygen assisted dissociation through the formation of methoxy intermediates involving O species derived from the oxidants (O_2, CO_2 or H_2O) or reactive oxygen species from the catalyst support [52]. Most reported mechanism and kinetic studies of DRM have reported the former route of direct dissociation of C-H bonds in methane on the metal surface to form $CH_x - *$ [45, 51]. But there are also ample examples in literature that indicate that methane activation and dissociation is assisted by oxygen species

from the support or reactants [42, 54, 56-58]. For example, Bitter et al. observed that the DRM activity of Pt/ZrO_2 catalysts could be correlated not with the Pt surface area but with the Pt/ZrO_2 interface, suggesting that the kinetically relevant step of DRM occurred at Pt/ZrO_2 interfacial sites [56]. Bradford et al. concluded that oxygen from the support in reducible supports like TiO_2 can participate in the activation of both CH_4 and CO_2 [54]. Lustemberg et al. [59] have proposed from AP-XPS observations and DFT calculations that on highly dispersed Ni/CeO_2 systems, the Ni and O centers of ceria work in a cooperative way in the dissociation of the C−H bond, with the proposed transition state of CH_4 having a coordination with both the Ni and O centers.

Hence, we propose that methane activation and dissociation in this Ni-PS@$Ce_{1-x}Zr_xO_2$ catalyst system occurs through an oxygen assisted route involving the lattice oxygen of the $Ce_{1-x}Zr_xO_2$ shell. The high level of encapsulation and interfacial contact of Ni nanoparticles with the redox support can promote the oxygen-assisted mechanism of CH_4 activation. The activation barrier of methane decomposition, thus, depends on the mobility and reactivity of the lattice oxygen and the degree of stabilization of the O-containing intermediate at the $Ni/Ce_{1-x}Zr_xO_2$ interface.

3.3.2.1. Methane-TPSR

A comparison of the light-off temperature for methane conversion during a temperature programmed surface reaction/ decomposition experiment for methane (CH_4-TPSR) between Ni-PS@$Ce_{0.9}Zr_{0.1}O_2$ and Ni-PS catalysts strongly supports this hypothesis (Figure 9). In this experiment, 20% CH_4 in Ar was passed over the reduced Ni-PS@$Ce_{0.9}Zr_{0.1}O_2$ and Ni-PS catalysts while the temperature was ramped up at a controlled rate.

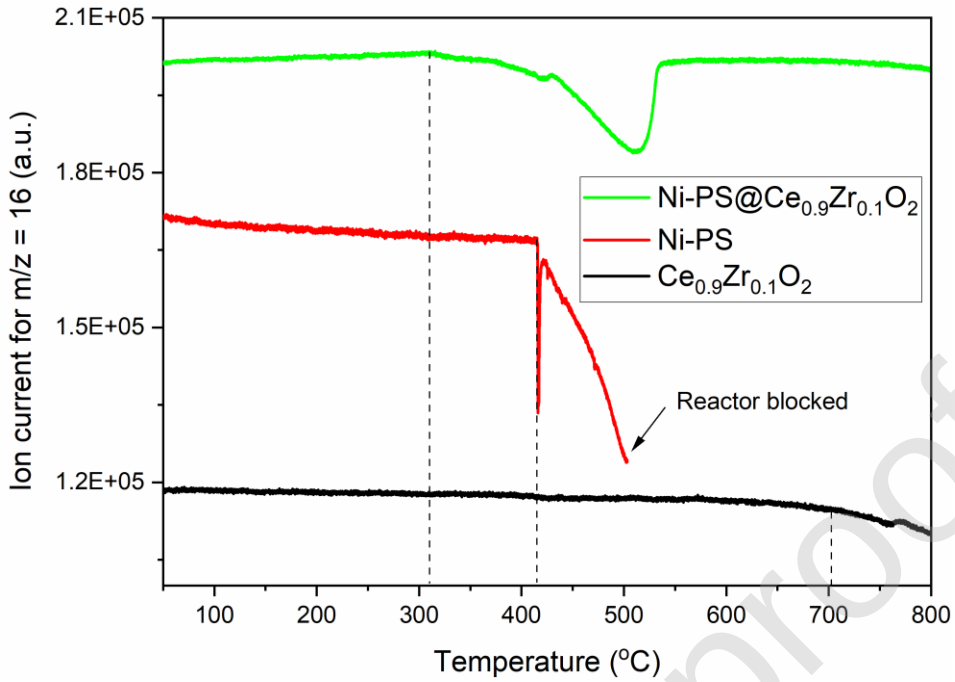

Figure 9. Mass spectrum for methane during CH_4-TPSR on reduced Ni-PS@$Ce_{0.9}Zr_{0.1}O_2$, Ni-PS and $Ce_{0.9}Zr_{0.1}O_2$.

It is observed that CH_4 conversion starts at a temperature of 310°C on the Ni-PS@$Ce_{0.9}Zr_{0.1}O_2$ catalyst (Figure 9), with a concurrent production of CO and CO_2 (Figure S20). On the other hand, the Ni-PS catalyst requires 415°C to start dissociating methane. CO/CO_2 formation is observed over an extended duration on Ni-PS@$Ce_{0.9}Zr_{0.1}O_2$ (over a temperature range of 300 – 440°C, until the exhaustion of the lattice oxygen pool of the support), whereas there is only a short sharp spike of CO, CO_2 formation on Ni-PS (likely associated with the reduction some residual NiO or hydroxyl groups in the catalyst), followed by production of only H_2. The significant lowering of the light-off methane conversion temperature on Ni-PS@$Ce_{0.9}Zr_{0.1}O_2$ (310°C) compared to Ni-PS (415°C) suggests that the lattice oxygen in the $Ce_{0.9}Zr_{0.1}O_2$ shell may play a role in activating and dissociating methane. A control CH_4-TPSR experiment using only $Ce_{0.9}Zr_{0.1}O_2$ shows negligible CH_4 conversion below 700°C [60]. The CH_4-TPSR results show that Ni is necessary

for CH_4 activation under the relatively lower temperature conditions, and the presence of lattice oxygen in the vicinity of the Ni sites facilitates methane activation.

3.3.2.2. Pulsed isotope experiments

To further demonstrate the role of lattice oxygen in methane activation on these catalysts, another experiment was conducted using pulses of the reactant gases to observe the effect of depletion/ fulfilling of lattice oxygen in Ni-PS@$Ce_{0.9}Zr_{0.1}O_2$ on its methane conversion activity in the absence of any other co-fed reactant (Figure 10). The aim of this experiment is not to conduct a detailed SSITKA analysis for DRM, as has been reported in several recent studies on supported catalysts [7-11], but to modulate the lattice oxygen pool in the catalyst and study its effect on the CH_4 conversion. In this experiment, the reduced Ni-PS@$Ce_{0.9}Zr_{0.1}O_2$ catalyst was exposed to the following sequence of pulses of equal volume at 600^{o}C: 1. five pulses of $^{13}CH_4$ (pulse #1-5), 2. three pulses of $^{12}CO_2$ (pulse #6-8), 3. three pulses of $^{13}CH_4$ (pulse #9-11), 4. three pulses of H_2 (pulse #12-14), and 5. three pulses of $^{13}CH_4$ (pulse #15-17). The conversions of $^{13}CH_4$ in each of these pulses are indicative of the methane dissociation activity of the catalyst in that pulse.

When $^{13}CH_4$ is pulsed on the freshly reduced catalyst (pulse #1-5), formation of H_2, ^{13}CO and $^{13}CO_2$ products are observed, clearly indicating that $^{13}CH_4$ is dissociated to form H_2 and ^{13}C-containing intermediates and these carbonaceous intermediates are oxidized by oxygen from the support. Similar observations have been reported by Vasiliades et al. in transient isotopic studies on supported Ni/ceria-zirconia catalysts [7]. The molar ratio of H_2 produced to $^{13}CH_4$ converted in the first pulse was calculated to be 1.14, which is much lower than the value of 2 expected from direct dissociation of methane to carbon and H_2. The selectivity of $^{13}CO_2$ formation

compared to ^{13}CO decreases with increasing methane pulses as lattice oxygen is progressively diminished.

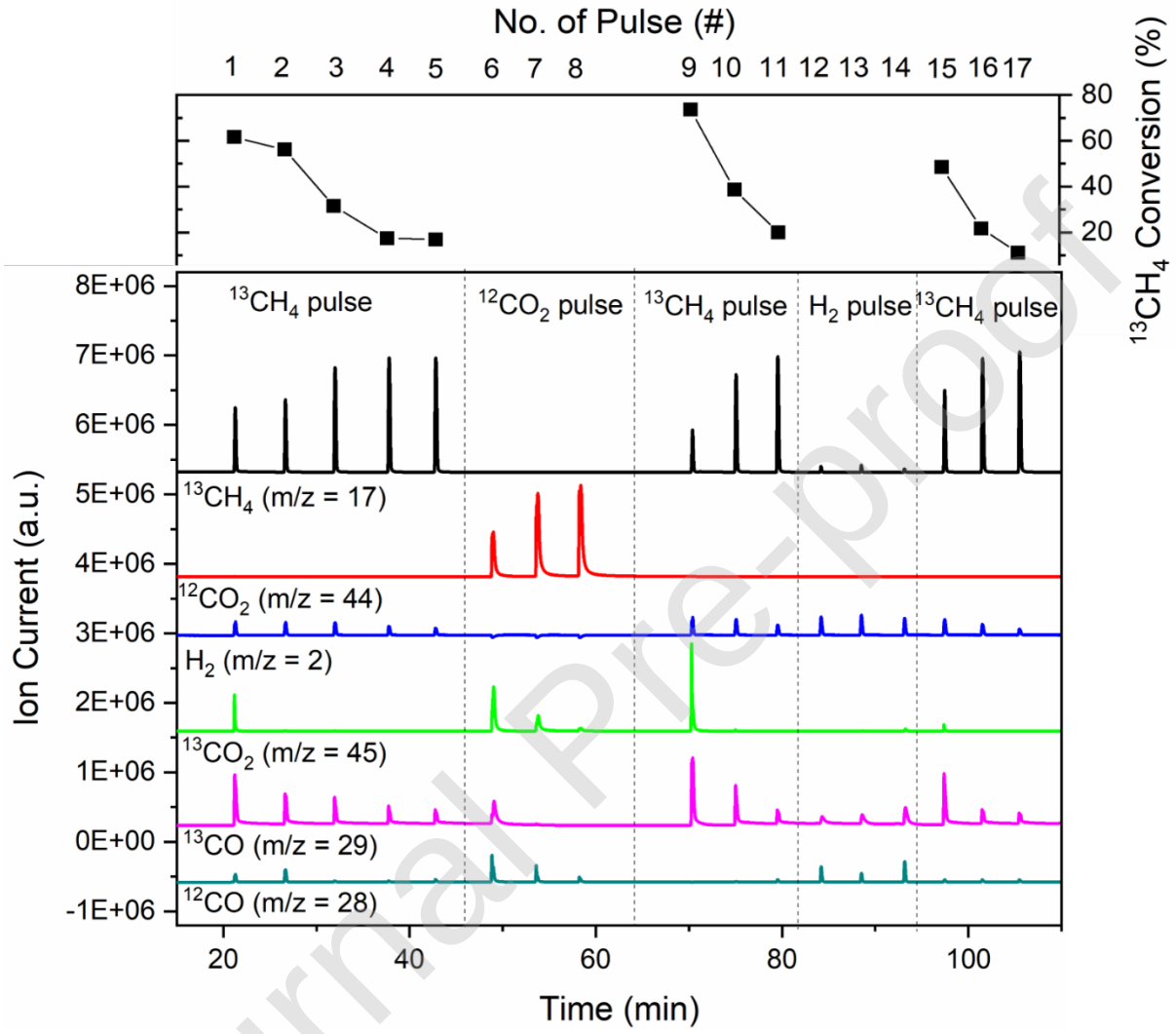

Figure 10. Mass spectra of outlet gas during pulsed isotopic experiments on reduced Ni-PS@$Ce_{0.9}Zr_{0.1}O_2$ at 600°C. The catalyst was reduced at 750°C in situ before purging with He and exposure to pulses (0.3 ml each) of $^{13}CH_4$ (pulse #1-5, 9-11, 15-17), CO_2 (pulse #6-8) and H_2 (pulse #12-14).

It is observed the conversion of $^{13}CH_4$ decreases ($^{13}CH_4$ peak area for outlet gas increases) over subsequent pulses (pulse #1-5), with a concurrent decrease in $^{13}CO_x$ formation. We note that over subsequent methane pulses, two factors can contribute to the gradual loss of CH_4 dissociation activity of the catalyst – 1. the coverage of active sites by coke from $^{13}CH_4$ decomposition, and 2.

the gradual depletion of the oxygen pool on the support. To investigate if the latter factor plays any role in the methane dissociation kinetics, two types of *in situ* catalyst regeneration was attempted – 1. introducing pulses of CO_2 (pulse #6-8), and 2. introducing pulses of H_2 (pulse #12-14). Both CO_2 and H_2 pulses at the reaction temperature are expected to remove the accumulated active carbon pool from the Ni sites in the form of CO_x or CH_4/C_xH_y species [9, 11] and thereby partially regenerate the available Ni surface. The two approaches however differ in the effect on the lattice oxygen content of the catalyst; CO_2 pulses are expected to replenish lattice oxygen whereas H_2 pulses should have the opposite effect. We observe that when CO_2 is pulsed following $^{13}CH_4$ (pulse #6-8), ^{12}CO is formed from the dissociation of $^{12}CO_2$ by backfilling oxygen vacancies in the catalyst, and $^{13}CO_x$ are formed by the oxidation of coke species. In the subsequent $^{13}CH_4$ pulse after the CO_2 regeneration (pulse #9), a significantly increased $^{13}CH_4$ conversion and higher $^{13}CO_x$ product formation is observed. It is worth noting that the $^{13}CH_4$ conversion in pulse #9 (74%) is higher than that on the freshly reduced catalyst (pulse #1, 61%). When H_2 pulses are introduced to regenerate the catalyst (pulse #12-14), evolution of $^{13}CH_4$ from hydrogenation of coke, and ^{12}CO and ^{13}CO, possibly from RWGS involving lattice oxygen/ surface carbonates, are observed. The $^{13}CH_4$ conversion activity of the catalyst is partially regenerated after the H_2 pulses, but the $^{13}CH_4$ conversion (pulse #15, 48%) is much lower than that after CO_2 pulses (pulse #9, 74%). The relative efficiency of coke removal by CO_2 pulses and H_2 pulses was examined by subjecting the catalyst after the CO_2/H_2 pulse regenerations to pulses of O_2 (in separate experiments). The residual coke species after the CO_2/H_2 treatments (inactive carbon) are removed in the form of $^{13}CO_2$ and ^{13}CO upon reaction with O_2. We observe that the amount of CO_x formed by the oxidation of residual coke is nearly same for the CO_2 and H_2 pulse regenerations (Figure S21), suggesting both treatments are

equally effective in removing the coke species. We, hence, propose that the increasing trend of CH_4 dissociation activity of the catalyst post H_2 pulse (pulse #15) < freshly reduced (pulse #1) < post CO_2 pulse (pulse #9) is caused by the increasing lattice oxygen pool available on the catalyst in the corresponding pulses, that helps in the activation and dissociation of methane.

We note that in this line of reasoning, we have not considered the electronic effects of exposing the catalyst to CO_2 or H_2 pulses on Ni and its chemical environment, which would require elaborate theoretical calculations. However, in general, metallic Ni^0 is more active for methane conversion than oxidized Ni^{2+}; and thus, further reduction of Ni valence state by H_2 treatment is expected to improve its catalytic activity compared to CO_2 treatment, that can partially oxidize the Ni surface. The observations in this pulsed experiment show an opposite effect, which we assign to the difference in lattice oxygen content of ceria-zirconia.

3.3.2.3. Kinetic Model

Based on the above considerations, the following reaction mechanism is proposed on the Ni-PS@$Ce_{0.9}Zr_{0.1}O_2$ catalyst:

$$CH_4 + * \overset{K_1}{\leftrightarrow} CH_4 - * \qquad (i)$$

$$CH_4 - * + 4\,O_x \overset{k_2}{\rightarrow} C - * + 4\,O_x - H \quad (RDS) \qquad (ii)$$

$$2\,O_x - H \overset{K_3}{\leftrightarrow} H_2 + 2\,O_x \qquad (iii)$$

$$C - * + O_x \overset{K_4}{\leftrightarrow} CO + O_{x-1} + * \qquad (iv)$$

$$CO_2 + O_{x-1} \overset{K_5}{\leftrightarrow} CO + O_x \qquad (v)$$

where * represents a surface Ni site, O_x represents lattice oxygen and O_{x-1} represents an oxygen vacancy.

The proposed mechanism is summarized as follows. Methane adsorption occurs on Ni in a quasi-equilibrium process. The adsorbed methane undergoes C-H bond dissociation through an O-containing intermediate such as methoxy intermediate (CH_xO-*) involving the lattice oxygen O_x of ceria-zirconia, eventually forming CH_x-* $(x = 3-0)$ and hydroxyl on ceria-zirconia [57]. This step of O-assisted methane dissociation is the RDS. It is to be noted that multiple elementary steps are involved in Eq. (ii), each involving the dissociation of one C-H bond. The activation barrier for the first C-H bond dissociation of CH_4 is probably the slowest step, with the subsequent C-H scissions being relatively faster and in a quasi-equilibrium state [59]. Eq. (ii) can hence be expanded into Eq. (vi) – (viii), and the quasi-equilibrium steps of sequential C-H bond cleavage of CH_x-* to $C-*$ may occur either though O-containing intermediates involving O_x (Eq. vii) [61] or by direct dehydrogenation (Eq. viii). However, each of these elementary steps are not considered separately in the kinetic model to avoid fitting of numerous kinetic and thermodynamic parameters that can lead to statistically insignificant parameter estimates. The lumped Eq. (ii) was considered as RDS for simplification, in line with previous literature reports [20]. Hydrogen product is produced by the scission of O-H bond and formation of H-H, followed by its desorption. $C-*$ intermediate formed from methane dissociation is oxidized by the lattice oxygen of ceria-zirconia to form CO and an oxygen vacancy O_{x-1}. For both step (ii) and (iv), it is important for the active lattice oxygen to diffuse from the bulk of the support (shell) to the Ni/ceria-zirconia interface [9] and possibly spill-over to the Ni surface to react with CH_x-Ni intermediates (and/or CH_x-Ni intermediate has to diffuse over the Ni surface to reach the Ni/ceria interface); thus, the oxygen mobility or the oxygen diffusion rate through the ceria-zirconia

lattice plays a key role in the activation barriers of these steps. The constants k_2 and K_4 are lumped parameters that include both the processes of lattice oxygen diffusion from bulk to the active centers and the reaction of lattice oxygen with the corresponding intermediates.

The oxygen vacancies formed after carbon gasification (Eq. (ii)) act as the activation centers for CO_2 dissociation [19, 58, 62]. CO_2 activation and dissociation may occur both on the support oxygen vacancies to form CO and lattice oxygen and on the Ni metal surface to form adsorbed CO-* and O-* intermediates. Vasiliades et al. [11] demonstrated via advanced transient isotopic experiments that on ceria-zirconia supported catalysts, the quantity of CO formation through the lattice oxygen route is much higher than that by CO_2 dissociation on the metal surface. Following their observations, we assume here that CO_2 dissociation on these catalysts primarily occurs directly on the oxygen vacancy following Eq. (v). Thus, the lattice oxygen in the ceria-zirconia shell is involved in the activation of both CH_4 and CO_2 in the proposed mechanism – with Ce^{3+}-O_{x-1} oxygen vacancy sites as the activation sites for CO_2 dissociation, and the O at Ni/ceria-zirconia interface accelerating C-H dissociation in CH_4.

$$CH_4 - * + O_x \xrightarrow{k_{2a}} CH_3 - * + O_x - H \quad (RDS) \qquad (vi)$$

$$CH_3 - * + O_x \overset{K_{2b}}{\leftrightarrow} CH_2 - * + O_x - H \Rightarrow CH_2 - * + O_x \overset{K_{2c}}{\leftrightarrow} CH - * + O_x - H$$

$$\Rightarrow CH - * + O_x \overset{K_{2d}}{\leftrightarrow} C - * + O_x - H \qquad (vii)$$

or,

$$CH_3 - * + * \overset{K_{2e}}{\leftrightarrow} CH_2 - * + H - * \Rightarrow CH_2 - * + * \overset{K_{2f}}{\leftrightarrow} CH - * + H - *$$

$$\Rightarrow CH - * + * \overset{K_{2g}}{\leftrightarrow} C - * + H - * \qquad (viii)$$

The rate equation for the above reaction mechanism is presented in Eq. 13.

$$r_f = \frac{A\exp(-E_A/RT)\,P_{CH_4}}{\left(1 + K_a\frac{P_{CO}}{P_{CO_2}} + K_b\,{P_{H_2}}^{0.5}\right)^4\left(1 + K_cP_{CH_4} + K_d\frac{{P_{CO}}^2}{P_{CO_2}}\right)} \qquad (13)$$

Where $K_a = 1/K_5$, $K_b = 1/{K_3}^{0.5}$, $K_c = K_1$; $K_d = 1/K_4K_5$, all equilibrium coefficients are estimated by the Van't Hoff equation $K_i = \exp\left(\frac{-\Delta H_i + T\Delta S_1}{RT}\right)$

and,

$$r_{CH_4} = \frac{A\exp(-E_A/RT)\,P_{CH_4}}{\left(1 + K_a\frac{P_{CO}}{P_{CO_2}} + K_b\,{P_{H_2}}^{0.5}\right)^4\left(1 + K_cP_{CH_4} + K_d\frac{{P_{CO}}^2}{P_{CO_2}}\right)}\left(1 - \frac{{P_{H_2}}^2{P_{CO}}^2}{K_{eq}P_{CH_4}P_{CO_2}}\right) \qquad (14)$$

The kinetic parameters were estimated by the minimization of errors between the experimental data and the kinetic model. An excellent fit was obtained with a correlation coefficient of close to unity (R^2 = 0.955) (Figure 11). The value of activation energy of DRM predicted by the model is 54.2 kJ mol^{-1}, which is reasonable and in line with previous literature reports [38, 44, 46, 63-65]. The estimated kinetic parameters for this model are tabulated in Table 4. Relatively high product inhibition terms are predicted by the kinetic model (relatively high value of K_d in the denominator, refer Table 4), indicating significant suppression of reaction rate at high CO product concentration. We also observe this product inhibition effect while testing DRM performance of these catalysts, where significant reductions have to be made in the space velocity to achieve high reactant conversion. Further studies are being conducted to better understand and unequivocally determine these inhibition terms and will be addressed in a future publication.

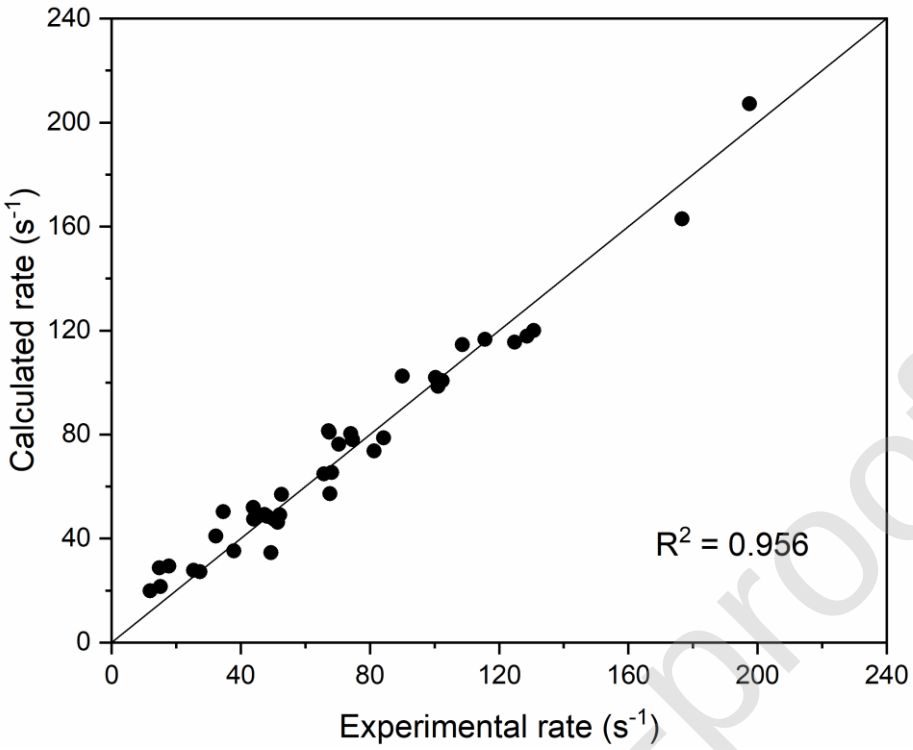

Figure 8. Parity plot of CH_4 conversion rate measured experimentally and calculated from kinetic model (Equation 14).

Table 4. Estimated kinetic parameters for proposed model.

Parameter	ΔS (J/mol K)	ΔH (kJ/mol)
K_a	-157	-104
K_b	-195	-163
K_c	-217	-200
K_d	-150	-172
	A (s^{-1} atm^{-1})	E_a (kJ/mol)
k	1.85E+06	54.2

Attempts were also made to fit some other reported kinetic models [20, 66-69] to the experimental data to compare the goodness of fit with our proposed model. The parity plots of the experimentally measured rates with those predicted from select reported models are

presented in Figure S22. The regression coefficients of these model fittings were markedly lower relative to our proposed model.

Thus, we propose that a Mars-van Krevelen type redox mechanism with a RDS of methane dissociation through intermediates involving lattice oxygen from ceria-zirconia is followed on Ni-PS@$Ce_{1-x}Zr_xO_2$ catalyst system. This results in a direct correlation between the oxygen mobility and storage capacity of the catalyst and the reaction rate of DRM. Since O_x is involved in the rate determining step, the mobility, activity and concentration of the redox-active oxygen species can directly affect the pre-exponential factor and activation energy of the reaction. The interface between Ni and ceria-zirconia, thus, becomes the catalytically active site for the kinetically relevant step, and an optimum level of SMSI that maximizes this interface, while allowing reactants to contact and adsorb on these sites, may be expected to maximize the DRM activity.

It is not clear whether the core-shell morphology of the system would make a difference on the favored reaction mechanism. In principle, the same mechanism may also be valid for conventional supported Ni/$Ce_{1-x}Zr_xO_2$ catalyst. But we note that the interface between the metal and the reducible oxide is higher in core-shell catalysts than supported ones. This high metal/support interface may be a driving factor behind the O-mediated CH_4 activation mechanism on these core-shell catalysts.

4. CONCLUSION

In this study, a series of Ni-PS@$Ce_{1-x}Zr_xO_2$ (x = 0 – 0.2) sandwiched core@shell catalysts are studied for DRM, and the effect of Zr doping on the physicochemical properties and DRM

performance of the catalyst is thoroughly analyzed. It is observed that a moderate amount of Ce substitution by Zr leads to significantly improved DRM activity, while not compromising on the excellent coke resistance and stability of the core-shell catalyst. The increased DRM activity is primarily assigned to an enhancement in oxygen storage capacity and interaction of Ni with ceria-zirconia, when optimum levels of Zr is incorporated in the ceria lattice. The core-shell morphology of the catalyst minimizes the effects of Zr doping on the textural properties of the catalyst and resistance to sintering or coke-formation, thereby allowing a unique opportunity to probe the fundamental dependence of DRM activity on the lattice oxygen content of ceria-zirconia. A detailed kinetic and mechanism study indicates that methane decomposition is the sole rate determining step for DRM on these catalysts. Based on CH_4-TPSR and pulsed isotopic experiments, we propose that the lattice oxygen of the ceria-zirconia at the interface with Ni is involved not only in oxidation of coke precursors but also in facilitating the rate determining step of methane dissociation by an oxygen-mediated dissociation pathway. The oxygen transport properties of the ceria-zirconia shell, thus, play a direct role in both the coke resistance and the catalytic activity for DRM. A significant product inhibition effect by CO on the reaction rate is predicted by the kinetic experiments. We believe that the insights gained from this study into the effect of oxygen storage properties of redox materials on the DRM reaction mechanism and kinetics can provide directions for future research in developing coke-resistant, stable, and highly active catalysts for DRM.

Credit Author Statement:

Sonali Das: Conceptualization, methodology, investigation, validation, writing – original draft preparation;

Ashok Jangam: Validation, writing – reviewing and editing;

Shanmukapriya Jayaprakash: investigation;

Shibo Xi: investigation;

Kus Hidajat: supervision;

Keiichi Tomishige: supervision, writing – reviewing and editing;

Sibudjing Kawi: supervision, writing – reviewing and editing, resources.

Declarations of interest: none

ACKNOWLEDGMENT

The research was supported by the National Environmental Agency of Singapore (NEA-ETRP Grant 1501 103), A*STAR (AME-IRG A1783c0016), and the Ministry of Education of Singapore (MOE2017-T2-2-130). The authors also gratefully thank the National University of Singapore for supporting the research.

REFERENCES

[1] Z. Bian, S. Das, M.H. Wai, P. Hongmanorom, S. Kawi, A Review on Bimetallic Nickel-Based Catalysts for CO2 Reforming of Methane, ChemPhysChem, 18 (2017) 3117-3134.

[2] Z. Li, S. Das, P. Hongmanorom, N. Dewangan, M.H. Wai, S. Kawi, Silica-based micro- and mesoporous catalysts for dry reforming of methane, Catalysis Science & Technology, 8 (2018) 2763-2778.

[3] S. Das, J. Pérez-Ramírez, J. Gong, N. Dewangan, K. Hidajat, B.C. Gates, S. Kawi, Core–shell structured catalysts for thermocatalytic, photocatalytic, and electrocatalytic conversion of CO2, Chemical Society Reviews, (2020).

[4] S. Das, A. Jangam, S. Xi, A. Borgna, K. Hidajat, S. Kawi, Highly Dispersed Ni/Silica by Carbonization–Calcination of a Chelated Precursor for Coke-Free Dry Reforming of Methane, ACS Applied Energy Materials, 3 (2020) 7719-7735.

[5] Z. Bian, I.Y. Suryawinata, S. Kawi, Highly carbon resistant multicore-shell catalyst derived from Ni-Mg phyllosilicate nanotubes@silica for dry reforming of methane, Applied Catalysis B: Environmental, 195 (2016) 1-8.

[6] S. Das, J. Ashok, Z. Bian, N. Dewangan, M.H. Wai, Y. Du, A. Borgna, K. Hidajat, S. Kawi, Silica–Ceria sandwiched Ni core–shell catalyst for low temperature dry reforming of biogas: Coke resistance and mechanistic insights, Applied Catalysis B: Environmental, 230 (2018) 220-236.

[7] M.A. Vasiliades, P. Djinović, L.F. Davlyatova, A. Pintar, A.M. Efstathiou, Origin and reactivity of active and inactive carbon formed during DRM over Ni/Ce0.38Zr0.62O2-δ studied by transient isotopic techniques, Catalysis Today, 299 (2018) 201-211.

[8] C.M. Damaskinos, M.A. Vasiliades, A.M. Efstathiou, The effect of Ti4+ dopant in the 5 wt% Ni/Ce1-xTixO2-δ catalyst on the carbon pathways of dry reforming of methane studied by various transient and isotopic techniques, Applied Catalysis A: General, 579 (2019) 116-129.

[9] M.A. Vasiliades, P. Djinović, A. Pintar, J. Kovač, A.M. Efstathiou, The effect of CeO2–ZrO2 structural differences on the origin and reactivity of carbon formed during methane dry reforming over NiCo/CeO2–ZrO2 catalysts studied by transient techniques, Catalysis Science & Technology, 7 (2017) 5422-5434.

[10] M.A. Vasiliades, C.M. Damaskinos, K.K. Kyprianou, M. Kollia, A.M. Efstathiou, The effect of Pt on the carbon pathways in the dry reforming of methane over Ni-Pt/Ce0.8Pr0.2O2-δ catalyst, Catalysis Today, 355 (2020) 788-803.

[11] M.A. Vasiliades, C.M. Damaskinos, P. Djinović, A. Pintar, A.M. Efstathiou, Dry reforming of CH4 over NiCo/Ce0.75Zr0.25O2-δ: The effect of Co on the site activity and carbon pathways studied by transient techniques, Catalysis Communications, 149 (2021) 106237.

[12] P. Djinović, I.G. Osojnik Črnivec, B. Erjavec, A. Pintar, Influence of active metal loading and oxygen mobility on coke-free dry reforming of Ni–Co bimetallic catalysts, Applied Catalysis B: Environmental, 125 (2012) 259-270.

[13] C. Jiang, M.R. Akkullu, B. Li, J.C. Davila, M.J. Janik, K.M. Dooley, Rapid screening of ternary rare-earth – Transition metal catalysts for dry reforming of methane and characterization of final structures, Journal of Catalysis, 377 (2019) 332-342.

[14] A. Kambolis, H. Matralis, A. Trovarelli, C. Papadopoulou, Ni/CeO2-ZrO2 catalysts for the dry reforming of methane, Applied Catalysis A: General, 377 (2010) 16-26.

[15] A. Wolfbeisser, O. Sophiphun, J. Bernardi, J. Wittayakun, K. Föttinger, G. Rupprechter, Methane dry reforming over ceria-zirconia supported Ni catalysts, Catalysis Today, 277 (2016) 234-245.

[16] F. Zhang, Z. Liu, X. Chen, N. Rui, L.E. Betancourt, L. Lin, W. Xu, C.-j. Sun, A.M.M. Abeykoon, J.A. Rodriguez, J. Teržan, K. Lorber, P. Djinović, S.D. Senanayake, Effects of Zr Doping into Ceria for the Dry Reforming of Methane over Ni/CeZrO2 Catalysts: In Situ Studies with XRD, XAFS, and AP-XPS, ACS Catalysis, 10 (2020) 3274-3284.

[17] S. Damyanova, B. Pawelec, K. Arishtirova, M.V.M. Huerta, J.L.G. Fierro, The effect of CeO2 on the surface and catalytic properties of Pt/CeO2–ZrO2 catalysts for methane dry reforming, Applied Catalysis B: Environmental, 89 (2009) 149-159.

[18] N. Laosiripojana, D. Chadwick, S. Assabumrungrat, Effect of high surface area CeO2 and Ce-ZrO2 supports over Ni catalyst on CH4 reforming with H2O in the presence of O2, H2, and CO2, Chemical Engineering Journal, 138 (2008) 264-273.

[19] M.M. Makri, M.A. Vasiliades, K.C. Petallidou, A.M. Efstathiou, Effect of support composition on the origin and reactivity of carbon formed during dry reforming of methane over 5wt% Ni/Ce1−xMxO2−δ (M=Zr4+, Pr3+) catalysts, Catalysis Today, 259 (2016) 150-164.

[20] E. Akpan, Y. Sun, P. Kumar, H. Ibrahim, A. Aboudheir, R. Idem, Kinetics, experimental and reactor modeling studies of the carbon dioxide reforming of methane (CDRM) over a new Ni/CeO2–ZrO2 catalyst in a packed bed tubular reactor, Chemical Engineering Science, 62 (2007) 4012-4024.

[21] J.W. Han, J.S. Park, M.S. Choi, H. Lee, Uncoupling the size and support effects of Ni catalysts for dry reforming of methane, Applied Catalysis B: Environmental, 203 (2017) 625-632.

[22] Z. Bian, S. Kawi, Preparation, characterization and catalytic application of phyllosilicate: A review, Catalysis Today, 339 (2020) 3-23.

[23] J.C. Park, H.J. Lee, J.U. Bang, K.H. Park, H. Song, Chemical transformation and morphology change of nickel–silica hybrid nanostructuresvia nickel phyllosilicates, Chemical Communications, (2009) 7345-7347.

[24] X. Kong, Y. Zhu, H. Zheng, X. Li, Y. Zhu, Y.-W. Li, Ni Nanoparticles Inlaid Nickel Phyllosilicate as a Metal–Acid Bifunctional Catalyst for Low-Temperature Hydrogenolysis Reactions, ACS Catalysis, 5 (2015) 5914-5920.

[25] H.-S. Roh, H.S. Potdar, K.-W. Jun, J.-W. Kim, Y.-S. Oh, Carbon dioxide reforming of methane over Ni incorporated into Ce–ZrO2 catalysts, Applied Catalysis A: General, 276 (2004) 231-239.

[26] I. Luisetto, S. Tuti, C. Romano, M. Boaro, E. Di Bartolomeo, J.K. Kesavan, S.S. Kumar, K. Selvakumar, Dry reforming of methane over Ni supported on doped CeO2: New insight on the role of dopants for CO2 activation, Journal of CO2 Utilization, 30 (2019) 63-78.

[27] J.A. Montoya, E. Romero-Pascual, C. Gimon, P. Del Angel, A. Monzón, Methane reforming with CO2 over Ni/ZrO2–CeO2 catalysts prepared by sol–gel, Catalysis Today, 63 (2000) 71-85.

[28] P. Muhammed Shafi, A. Chandra Bose, Impact of crystalline defects and size on X-ray line broadening: A phenomenological approach for tetragonal SnO2 nanocrystals, AIP Advances, 5 (2015) 057137.

[29] B. Nematollahi, M. Rezaei, E.N. Lay, Preparation of highly active and stable NiO–CeO2 nanocatalysts for CO selective methanation, International Journal of Hydrogen Energy, 40 (2015) 8539-8547.

[30] K. Wu, L.-D. Sun, C.-H. Yan, Ceria-Based Nanocatalysts: Recent Progress in Well-Controlled Synthesis of Ceria-Based Nanocatalysts towards Enhanced Catalytic Performance (Adv. Energy Mater. 17/2016), Advanced Energy Materials, 6 (2016).

[31] C. Zhao, Q. Hao, Q. Zhang, N. Yan, J. Liu, B. Dou, F. Bin, Catalytic self-sustained combustion of toluene and reaction pathway over CuxMn1-xCe0.75Zr0.25/TiO2 catalysts, Applied Catalysis A: General, 569 (2019) 66-74.

[32] J. He, P. Yao, J. Qiu, H. Zhang, Y. Jiao, J. Wang, Y. Chen, Enhancement effect of oxygen mobility over Ce0.5Zr0.5O2 catalysts doped by multivalent metal oxides for soot combustion, Fuel, 286 (2021) 119359.

[33] Z. Wu, M. Li, J. Howe, H.M. Meyer, S.H. Overbury, Probing Defect Sites on CeO2 Nanocrystals with Well-Defined Surface Planes by Raman Spectroscopy and O2 Adsorption, Langmuir, 26 (2010) 16595-16606.

[34] W.-J. Jang, H.-M. Kim, J.-O. Shim, S.-Y. Yoo, K.-W. Jeon, H.-S. Na, Y.-L. Lee, D.-W. Jeong, J.W. Bae, I.W. Nah, H.-S. Roh, Key properties of Ni–MgO–CeO2, Ni–MgO–ZrO2, and Ni–MgO–Ce(1−x)Zr(x)O2 catalysts for the reforming of methane with carbon dioxide, Green Chemistry, 20 (2018) 1621-1633.

[35] D. He, H. Hao, D. Chen, J. Liu, J. Yu, J. Lu, F. Liu, G. Wan, S. He, Y. Luo, Synthesis and application of rare-earth elements (Gd, Sm, and Nd) doped ceria-based solid solutions for methyl mercaptan catalytic decomposition, Catalysis Today, 281 (2017) 559-565.

[36] L.P. Matte, A.S. Kilian, L. Luza, M.C.M. Alves, J. Morais, D.L. Baptista, J. Dupont, F. Bernardi, Influence of the CeO2 Support on the Reduction Properties of Cu/CeO2 and Ni/CeO2 Nanoparticles, The Journal of Physical Chemistry C, 119 (2015) 26459-26470.

[37] S. Bernal, J.J. Calvino, M.A. Cauqui, J.M. Gatica, C. Larese, J.A. Pérez Omil, J.M. Pintado, Some recent results on metal/support interaction effects in NM/CeO2 (NM: noble metal) catalysts, Catalysis Today, 50 (1999) 175-206.

[38] M. Li, A.C. van Veen, Tuning the catalytic performance of Ni-catalysed dry reforming of methane and carbon deposition via Ni-CeO2-x interaction, Applied Catalysis B: Environmental, 237 (2018) 641-648.

[39] J.H. Bitter, K. Seshan, J.A. Lercher, The State of Zirconia Supported Platinum Catalysts for CO2/CH4Reforming, Journal of Catalysis, 171 (1997) 279-286.

[40] M. Cargnello, V.V.T. Doan-Nguyen, T.R. Gordon, R.E. Diaz, E.A. Stach, R.J. Gorte, P. Fornasiero, C.B. Murray, Control of Metal Nanocrystal Size Reveals Metal-Support Interface Role for Ceria Catalysts, Science, 341 (2013) 771.

[41] V. Sadykov, V. Muzykantov, A. Bobin, N. Mezentseva, G. Alikina, N. Sazonova, E. Sadovskaya, L. Gubanova, A. Lukashevich, C. Mirodatos, Oxygen mobility of Pt-promoted doped CeO2–ZrO2 solid solutions: Characterization and effect on catalytic performance in syngas generation by fuels oxidation/reforming, Catalysis Today, 157 (2010) 55-60.

[42] M. Zhang, J. Zhang, Z. Zhou, S. Chen, T. Zhang, F. Song, Q. Zhang, N. Tsubaki, Y. Tan, Y. Han, Effects of the surface adsorbed oxygen species tuned by rare-earth metal doping on dry reforming of methane over Ni/ZrO2 catalyst, Applied Catalysis B: Environmental, 264 (2020) 118522.

[43] B. Safavinia, Y. Wang, C. Jiang, C. Roman, P. Darapaneni, J. Larriviere, D.A. Cullen, K.M. Dooley, J.A. Dorman, Enhancing CexZr1−xO2 Activity for Methane Dry Reforming Using Subsurface Ni Dopants, ACS Catalysis, 10 (2020) 4070-4079.

[44] M.C.J. Bradford, M.A. Vannice, CO2 Reforming of CH4, Catalysis Reviews, 41 (1999) 1-42.

[45] Y. Kathiraser, U. Oemar, E.T. Saw, Z. Li, S. Kawi, Kinetic and mechanistic aspects for CO2 reforming of methane over Ni based catalysts, Chemical Engineering Journal, 278 (2015) 62-78.

[46] J. Wei, E. Iglesia, Isotopic and kinetic assessment of the mechanism of reactions of CH4 with CO2 or H2O to form synthesis gas and carbon on nickel catalysts, Journal of Catalysis, 224 (2004) 370-383.

[47] L.N. Bobrova, A.S. Bobin, N.V. Mezentseva, V.A. Sadykov, J.W. Thybaut, G.B. Marin, Kinetic assessment of dry reforming of methane on Pt+Ni containing composite of fluorite-like structure, Applied Catalysis B: Environmental, 182 (2016) 513-524.

[48] A. Jangam, S. Das, N. Dewangan, P. Hongmanorom, W.M. Hui, S. Kawi, Conversion of CO2 to C1 chemicals: Catalyst design, kinetics and mechanism aspects of the reactions, Catalysis Today, (2019).

[49] J. Niu, S.E. Liland, J. Yang, K.R. Rout, J. Ran, D. Chen, Effect of oxide additives on the hydrotalcite derived Ni catalysts for CO2 reforming of methane, Chemical Engineering Journal, 377 (2019) 119763.

[50] J. Toyir, P. Gélin, H. Belatel, A. Kaddouri, Ir/Ce0.9Gd0.1O2−x as a new potential anode component in solid oxide fuel cells integrating the concept of gradual internal reforming of methane, Catalysis Today, 157 (2010) 451-455.

[51] J. Wei, E. Iglesia, Structural requirements and reaction pathways in methane activation and chemical conversion catalyzed by rhodium, Journal of Catalysis, 225 (2004) 116-127.

[52] D. Pakhare, J. Spivey, A review of dry (CO2) reforming of methane over noble metal catalysts, Chemical Society Reviews, 43 (2014) 7813-7837.

[53] V.A. Tsipouriari, X.E. Verykios, Kinetic study of the catalytic reforming of methane with carbon dioxide to synthesis gas over Ni/La2O3 catalyst, Catalysis Today, 64 (2001) 83-90.

[54] M.C.J. Bradford, M. Albert Vannice, The role of metal–support interactions in CO2 reforming of CH4, Catalysis Today, 50 (1999) 87-96.

[55] X. Fang, J. Zhang, J. Liu, C. Wang, Q. Huang, X. Xu, H. Peng, W. Liu, X. Wang, W. Zhou, Methane dry reforming over Ni/Mg-Al-O: On the significant promotional effects of rare earth Ce and Nd metal oxides, Journal of CO2 Utilization, 25 (2018) 242-253.

[56] J.H. Bitter, K. Seshan, J.A. Lercher, On the contribution of X-ray absorption spectroscopy to explore structure and activity relations of Pt/ZrO2 catalysts for CO2/CH4 reforming, Topics in Catalysis, 10 (2000) 295-305.

[57] A. Erdohelyi, J. Cserenyi, F. Solymosi, Activation of CH4 and Its Reaction with CO2 over Supported Rh Catalysts, Journal of Catalysis, 141 (1993) 287-299.

[58] I.V. Yentekakis, G. Goula, M. Hatzisymeon, I. Betsi-Argyropoulou, G. Botzolaki, K. Kousi, D.I. Kondarides, M.J. Taylor, C.M.A. Parlett, A. Osatiashtiani, G. Kyriakou, J.P. Holgado, R.M. Lambert, Effect of support oxygen storage capacity on the catalytic performance of Rh nanoparticles for CO2 reforming of methane, Applied Catalysis B: Environmental, 243 (2019) 490-501.

[59] P.G. Lustemberg, P.J. Ramírez, Z. Liu, R.A. Gutiérrez, D.G. Grinter, J. Carrasco, S.D. Senanayake, J.A. Rodriguez, M.V. Ganduglia-Pirovano, Room-Temperature Activation of Methane and Dry Re-forming with CO2 on Ni-CeO2(111) Surfaces: Effect of Ce3+ Sites and Metal–Support Interactions on C–H Bond Cleavage, ACS Catalysis, 6 (2016) 8184-8191.

[60] N. Laosiripojana, S. Assabumrungrat, Catalytic dry reforming of methane over high surface area ceria, Applied Catalysis B: Environmental, 60 (2005) 107-116.

[61] Y. Tang, Y. Wei, Z. Wang, S. Zhang, Y. Li, L. Nguyen, Y. Li, Y. Zhou, W. Shen, F.F. Tao, P. Hu, Synergy of Single-Atom Ni1 and Ru1 Sites on CeO2 for Dry Reforming of CH4, Journal of the American Chemical Society, 141 (2019) 7283-7293.

[62] Z. Liu, D.C. Grinter, P.G. Lustemberg, T.-D. Nguyen-Phan, Y. Zhou, S. Luo, I. Waluyo, E.J. Crumlin, D.J. Stacchiola, J. Zhou, J. Carrasco, H.F. Busnengo, M.V. Ganduglia-Pirovano, S.D. Senanayake, J.A. Rodriguez, Dry Reforming of Methane on a Highly-Active Ni-CeO2 Catalyst: Effects of Metal-Support Interactions on C−H Bond Breaking, Angewandte Chemie International Edition, 55 (2016) 7455-7459.

[63] C. Pichas, P. Pomonis, D. Petrakis, A. Ladavos, Kinetic study of the catalytic dry reforming of CH4 with CO2 over La2−xSrxNiO4 perovskite-type oxides, Applied Catalysis A: General, 386 (2010) 116-123.

[64] A. Nandini, K.K. Pant, S.C. Dhingra, Kinetic study of the catalytic carbon dioxide reforming of methane to synthesis gas over Ni-K/CeO2-Al2O3 catalyst, Applied Catalysis A: General, 308 (2006) 119-127.

[65] Z. Zhang, X.E. Verykios, Mechanistic aspects of carbon dioxide reforming of methane to synthesis gas over Ni catalysts, Catalysis Letters, 38 (1996) 175-179.

[66] G.R. Moradi, M. Rahmanzadeh, S. Sharifnia, Kinetic investigation of CO2 reforming of CH4 over La–Ni based perovskite, Chemical Engineering Journal, 162 (2010) 787-791.

[67] S.Y. Foo, C.K. Cheng, T.-H. Nguyen, A.A. Adesina, Kinetic study of methane CO2 reforming on Co–Ni/Al2O3 and Ce–Co–Ni/Al2O3 catalysts, Catalysis Today, 164 (2011) 221-226.

[68] Z.L. Zhang, X.E. Verykios, Carbon dioxide reforming of methane to synthesis gas over supported Ni catalysts, Catalysis Today, 21 (1994) 589-595.

[69] A. Yamaguchi, E. Iglesia, Catalytic activation and reforming of methane on supported palladium clusters, Journal of Catalysis, 274 (2010) 52-63.